Acta Materialia 221 (2021) 117380

Contents lists available at ScienceDirect

Acta Materialia

journal homepage: www.elsevier.com/locate/actamat

Full length article

Role of local chemical fluctuations in the shock dynamics of medium entropy alloy CoCrNi

Zhuocheng Xie[a,b], Wu-Rong Jian[c,*], Shuozhi Xu[c], Irene J. Beyerlein[c,d], Xiaoqing Zhang[a], Zhihua Wang[e,*], Xiaohu Yao[a,b,*]

[a] State Key Laboratory of Subtropical Building Science, South China University of Technology, Guangzhou, Guangdong 510640, P. R. China
[b] Department of Engineering Mechanics, South China University of Technology, Guangzhou, Guangdong 510640, P. R. China
[c] Department of Mechanical Engineering, University of California, Santa Barbara, California 93106-5070, USA
[d] Materials Department, University of California, Santa Barbara, California 93106-5050, USA
[e] Institute of Applied Mechanics, College of Mechanical and Vehicle Engineering, Taiyuan University of Technology, Taiyuan, 030024, P. R. China

ARTICLE INFO

Article history:
Received 5 May 2021
Revised 2 October 2021
Accepted 5 October 2021
Available online 13 October 2021

Keywords:
Shock response
Defect evolution
Lattice distortion
Chemical short-range order
Medium entropy alloy

ABSTRACT

In this work, molecular dynamics simulations are conducted to investigate the shock responses and corresponding deformation mechanisms in single crystalline (SC) and nanocrystalline (NC) microstructure of the medium entropy alloy (MEA) CoCrNi. The effects of lattice distortion (LD) and chemical short-range order (CSRO) on the shock wave propagation, defect evolution, and the cavitation process are explored to distinguish the unique shock properties of MEA. The results reveal an anomalous anisotropy in the Hugoniot elastic limit different from that seen in pure FCC metals since LD reduces the barrier for Shockley partial (SP) formation but increases the resistance for SP propagation. With sufficient dislocations nucleated in the first shock compression stage, LD aids in the formation of nanotwins by slowing down dislocation propagation in the following release and tension stages. However, because a higher degree of CSRO increases the average intrinsic stacking fault energy above that of the random material, more stacking faults annihilate in the release stage, reducing the chances for nanotwinning. We show that voids prefer to nucleate at Ni segregation sites (with high CSRO) due to the large hydrostatic tensile strain created by the lattice mismatch between the neighboring Ni and CoCr regions, and moreover, the nucleation event favors the grain boundary during spallation in NCs.

© 2021 Acta Materialia Inc. Published by Elsevier Ltd. All rights reserved.

1. Introduction

In 2004, Yeh et al. [1] and Cantor et al. [2] independently proposed that stable single-phase solid solutions can be produced by tuning the configurational entropy of a nominally equi-atomic multi-element alloy system. Since then, the number of families of such multi-principal element alloys (MPEAs) has greatly expanded. They can include either alloy systems with four to six principal elements, like the originally proposed high entropy alloys (HEAs) [1,2], or with three elements, often referred to as medium entropy alloys (MEAs) [3]. MPEAs have displayed extraordinary mechanical properties, such as high strength [4–6], excellent corrosion and irradiation resistance [7–10], outstanding fracture toughness [11–13], and remarkable fatigue and creep resistance [14–18], making them promising candidates for next-generation structural materials. The MEA, CoCrNi, in particular, is one representative FCC MPEA that has demonstrated exceptional tensile strength, ductility and toughness under quasic-static loading [12,13,19,20], excellent performance at low temperatures [3,13,21], and a desirable combination of high shear strength and uniform shear strain under dynamic shear loading [22].

To date, the mechanical properties of MPEAs have been mainly studied under quasi-static loading with strain rates, usually ranging from 10^{-4} s^{-1} to 10^{-1} s^{-1}, [21,23–29]. Future transportation and defense technologies, however, demand structural materials that are also robust in extreme environments, involving dynamic loading. In view of their excellent performance under the quasi-static loading, it is vital to also investigate the dynamic properties of MPEAs.

In this regard, some research studies have focused on the medium high-rate behavior of MPEAs, using the Split Hopkinson Pressure Bar laboratory testing apparatus [30–36]. Dynamic

* Corresponding authors.
E-mail addresses: wurong@ucsb.edu (W.-R. Jian), wangzh@tyut.edu.cn (Z. Wang), yaoxh@scut.edu.cn (X. Yao).

https://doi.org/10.1016/j.actamat.2021.117380
1359-6454/© 2021 Acta Materialia Inc. Published by Elsevier Ltd. All rights reserved.

compression, tension and compression/tension shear-coupling experiments under medium-high strain-rates, ranging from 10^3 s^{-1} to 10^4 s^{-1} [37–40] are possible with this set up. By comparing quasi-static and dynamic compression responses, studies using Hopkinson Pressure Bar have reported high strain-rate sensitivity in face-centered cubic (FCC) HEAs (e.g., FeCoNiCrMn [30,34,41] and $Al_{0.1}$CrFeCoNi [31,42]), body-centered cubic (BCC) HEAs (e.g., $AlCoCrFeNiTi_x$ (x = 0, 0.2, 0.4) [33] and $AlCoCr_{1.5}Fe_{1.5}NiTi_{0.5}$ [32]) and FCC/BCC bi-phase HEAs (e.g., $AlCrCuFeNi_2$ [36] and $Al_{0.6}$CoCrFeNi [43]). Dynamic compression, compared with quasi-static compression, tends to generate dislocation networks and forest dislocations in $Al_{0.1}$CrFeCoNi and $Al_{0.6}$CoCrFeNi HEAs, which impede the dynamic recovery of dislocations and, thus, enhance the strain hardening rate [42,43]. With such high rates, nanoscale twinning is observed to become even more prevalent in FCC HEAs, like FeCoNiCrMn [30,34,43] and $Al_{0.1}$CrFeCoNi [31,42], or in the FCC phase of FCC/BCC dual phase HEAs, e.g., $Al_{0.6}$CoCrFeNi [43]. Dynamic tension and shear tests by Hopkinson Bar have revealed that the simultaneous high strength–high ductility combination seen in the FCC NiCoCrFe HEA in dynamic tensile loading originates from both dynamically formed nanoscale twins and the entanglement between dislocations and planar faults [44]. They further reported high notch strength in the same HEA by dynamic tension-shear loading [45]. Ma et al. [22] investigated the dynamic shear deformation of CoCrNi MEA and found that grain refinement, deformation twins, and the strong interactions between dislocations and twin boundaries contribute to enhancing strain hardening. However, a moderate thermal-softening effect, which postpones shear localization and subsequent adiabatic shear banding, was also observed in some FCC HEAs, including NiCoCrFeMn [46] and $Al_{0.3}$CrFeCoNi [47]. Thus, in these HEAs, dynamic shear loading, compared to quasi-static shear test, leads to a reduction in strain hardening. Zhao et al. [48] reported that amorphous islands can be generated in CrMnFeCoNi HEA at regions where a critical defect density is reached under a dynamic shear test. These regions can promote additional strengthening and/or toughening mechanisms to further enhance their resistance to extreme loading conditions.

Further increases in strain rate can be realized by gas-gun driven (10^5 s^{-1} - 10^8 s^{-1}) [49] or laser driven systems (over 10^9 s^{-1}) [50]. Both facilities produce a uniaxial strain state in the material and induce the shock wave propagation between the sample surfaces. Behind the shock wave front, various defects, such as dislocation, stacking faults (SFs) and twins, nucleate and evolve, depending on the crystallographic orientation distribution (texture) and starting microstructure. After the compression wave is reflected at the rear free surface, the pressure is released to zero, prior to the encounter with the release tail of the compression wave. Later, the interaction of these two rarefaction waves generates a tensile region, which may lead to the separation of material by micro-crack propagation (brittle failure) or void nucleation and coalescence (ductile failure) once a critical stress value, called the spall strength, is reached. Compared with medium strain rate loading, studies involving high strain rate loading of MPEAs under strain rates beyond 10^5 s^{-1} have rarely been conducted [51]. Jiang et al. [52] performed normal plate impact experiments on FCC CrMnFeCoNi and BCC NiCoFeCrAl alloys and reported exceptionally high Hugoniot elastic limits (HELs) and phase transition threshold stresses. Yang et al. [53,54] studied the effect of martensite content on the spallation damage evolution in an $Fe_{50}Mn_{30}Co_{10}Cr_{10}$ HEA, finding that large-sized and densely distributed martensitic areas limit void growth and alter void coalescence or microcrack propagation paths, leading to higher spall strengths.

Studies using molecular dynamics (MD) simulations, typically at high rates, and experimental tests, often at quasi-static rates, have similarly reported the strong influence of the local heterogeneities characteristic of HEAs and MEAs, especially lattice distortion (LD) and chemical short-range order (CSRO), which originates from the difference of atomic size among adjacent atoms and the preference for certain types of bonds within the first few neighbor shells, respectively [55–67]. According to these studies, local chemical environment within MPEAs complicates the pathways taken by gliding dislocations [68] and leads to a dispersion in the critical stresses needed to activate them [69,70]. Specifically, it has been reported that LD lowers the stress to form Shockley partials (SP) and CSRO influences SP nucleation sites by providing preferential nucleation regions [71]. Increases in both LD and the degree of CSRO increased the resistance to SP propagation.

Although the influences of local chemical environment on defect evolution have been discussed by quasi-static experiments and simulations at constant strain rate, their roles in deformation and spallation mechanisms under shock loading have yet to be investigated. Compared to quasi-static loading, defect evolution under shock loading with ultra-high strain rates and tri-axial stress state generated in uniaxial strain (i.e., one-dimensional) shock can be more sophisticated since the material undergoes inhomogeneous local stress state as shock wave propagates, reflects and interacts in the material, leading to varied spallation properties. Thus, the effect of LD and CSRO during different deformation stages and the correlation of deformation mechanisms between these stages and the resulting spallation are relevant issues that require further investigation for MPEAs.

Accordingly, in this work, using both hybrid Monte Carlo/MD and large-scale MD simulations, we investigate the roles LD and CSRO play on the shock responses and underlying defect evolution of both single crystal (SC) and nanocrystalline (NC) CoCrNi. In efforts to separate the effects of LD and CSRO, a suite of calculations are carried out at two temperatures, 1 K and 300 K, and repeated for a hypothetical *A*-atom material, a pure metal form that bears the average intrinsic properties of CoCrNi. We study the effect of SC shock loading orientation on the HEL and show that LD and CSRO can result in a reverse anisotropy from previous reports on pure metals and from results on the reference *A*-atom material. We characterize the defect evolution in every stage of shock testing. The first compression stage is characterized by the onset of dislocation nucleation and glide processes, which govern the value of the HEL. The subsequent release stage involves the formation of nanotwins and the accumulation of sessile dislocations from the multiple defect reactions that take place. At the tension stage, in the SC MEAs, once the material reaches the spall strength, the void starts to nucleate at Ni segregation regions either from the intersection sites of SFs or the shock-induced amorphous regions formed at the preceding compression stage, where severe hydrostatic strain is generated. In the NC MEAs, the triple GB junctions with Ni segregation serve as void initiation sites and the alloy subsequently fails by GB separation where Ni has segregated.

2. Methodology

The large-scale atomic/molecular massively parallel simulator (LAMMPS) is used for all MD simulations here [72]. The atomic interactions within the MEA Co-Cr-Ni system are described by the EAM interatomic potential developed by Li et al [57]. This potential has been successfully used in a few recent MD studies on the melting process [73] and defect evolution [57,59,71]. We also employed an *A*-atom EAM potential developed in our recent work [71] to create the hypothetical pure *A*-atom metal, which possesses average properties of the random MEA.

The simulation model systems contain about one million atoms for the SC models with dimensions of ~ 100 nm × 10.5 nm × 10.5 nm, and about three million atoms for the NC models with dimensions of ~ 102 nm × 18 nm × 18 nm. All shock simula-

Table 1
Schmid factors for the 12 slip systems for the [1$\bar{1}$0] and [111] loading orientations.

Orientation/Slip system	$\frac{(111)}{[01\bar{1}]}$	$\frac{(111)}{[10\bar{1}]}$	$\frac{(111)}{[1\bar{1}0]}$	$\frac{(\bar{1}11)}{[01\bar{1}]}$	$\frac{(\bar{1}11)}{[\bar{1}01]}$	$\frac{(\bar{1}11)}{[\bar{1}10]}$	$\frac{(\bar{1}\bar{1}1)}{[\bar{1}\bar{1}0]}$	$\frac{(\bar{1}\bar{1}1)}{[\bar{1}01]}$	$\frac{(\bar{1}\bar{1}1)}{[1\bar{1}0]}$	$\frac{(1\bar{1}1)}{[\bar{1}\bar{1}0]}$	$\frac{(1\bar{1}1)}{[01\bar{1}]}$	$\frac{(1\bar{1}1)}{[\bar{1}10]}$
[1$\bar{1}$0]	0	0	0	0.408	0.408	0	0.408	0.408	0	0	0	0
[111]	0	0	0	0	0.272	0.272	0.272	0.272	0	0.272	0	0.272

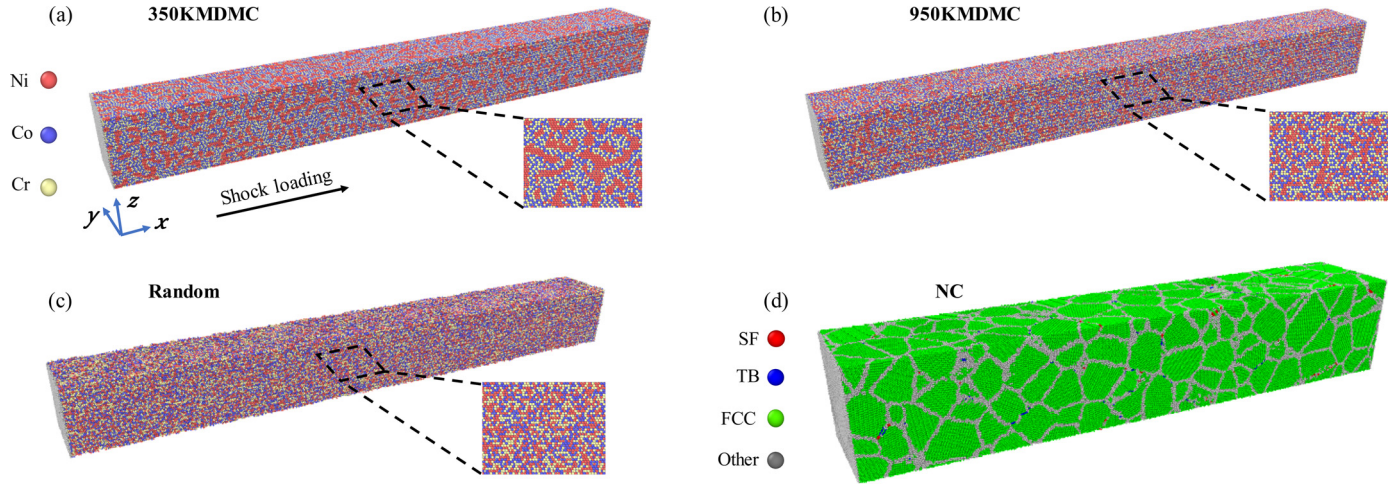

Fig. 1. (a)-(c) The representative atomic configurations for single crystalline (SC) 350KMDMC, 950KMDMC and random CoCrNi models, respectively. Here, 350KMDMC and 950KMDMC denote the models annealed at 350 K and 950 K during the hybrid MD/MC simulations, respectively. Random refers to the model material with an ideally random atomic distribution. (d) The atomic configurations of the model nanocrystal (NC) CoCrNi. Face-centered cubic (FCC), twin boundary (TB), stacking fault (SF), and atoms with unknown coordination structure are colored by green, blue, red, and gray, respectively. (For interpretation of the references to colour in this figure legend, the reader is referred to the web version of this article.)

tions are conducted along the *x*-axis. To examine anisotropy in the HEL, the SC model is either oriented with its [1$\bar{1}$0], [11$\bar{2}$] and [111] aligned respectively with the *x*-, *y*- and *z*-axes in the case of [1$\bar{1}$0] shock direction or with its [111], [1$\bar{1}$0] and [11$\bar{2}$] respectively aligned along *x*-, *y*- and *z*-axes in the case of [111] shock direction. The Schmid factors for these two orientations under uni-*x*-axis shock loading are provided in Table 1. We selected these two cases since the [111]-orientation is known as a geometrically hard orientation and [1$\bar{1}$0]-orientation, a geometrically medium one. For the NC model, we use the Poisson-Voronoi tessellation method [74] to generate 17 × 3 × 3 randomly oriented grains with an average size of ∼ 7.4 nm.

The equiatomic random CoCrNi MEA models are created by starting with only Ni element, followed by substituting the Ni atoms randomly by either Co or Cr atoms. For the construction of MEAs with different degrees of CSRO, a hybrid MD and MC simulation method is utilized under two different annealing temperatures (350 and 950 K), following the methods in [71]. We use 'number+K+MDMC' to denote the sample obtained by hybrid MD/MC simulation at a specific annealing temperature. The *A*-atom alloys are constructed by replacing all Ni atoms in the pure Ni models with *A*-atoms.

Fig. 1 shows the MEA microstructures for the SCs and NC. In these, the CSRO is measured by Warren-Cowley SRO parameters, $\alpha_{ij}^{n} = \frac{p_{ij}^{n} - c_j}{\delta_{ij} - c_j}$, where n means the nth nearest-neighbor shell of the central i-type atom, p_{ij}^{n} denotes the probability of a j-type atom being around an atom of type i within the nth shell, c_j is the concentration of j-type atom, and δ_{ij} is the Kronecker delta function [75,76]. The average LD is quantified based on calculating and comparing the radial distribution functions (RDF) $g(r)$ of this MEA sample and its *A*-atom counterpart. The difference in the full width at half maximum (FWHM) of the $g(r)$ curves between the MEA sample and the *A*-atom sample represents the LD of MEA. Detailed elaborations of CSRO by α_{ij}^{1} and the quantification of LD through RDF are illustrated in Figure S1 of the supplementary material. The corresponding values are shown in Table 2 and Table 3, respectively. According to Table 2, the random model in Fig. 1(c) has the CSRO parameters that are close to zero, indicating there is no CSRO. The lower annealing temperature case of the 350KMDMC sample possesses the highest degree of CSRO (Fig. 1(a)), with the largest absolute values of both $\alpha_{\mathrm{CoCr}}^{1}$ and $\alpha_{\mathrm{NiNi}}^{1}$ among the three MEA materials. In Table 3, we find that LD of MEA sample, i.e., the difference in the FWHMs of MEA and *A*-atom sample, is large at 1 K but moderate at 300 K. At any given temperature, the effect of CSRO on LD is slight, and overall, the LDs among MEAs at a given temperature are nearly the same.

To investigate the respective role of LD and CSRO, shock simulations are conducted for the SC *A*-atom, 350KMDMC, 950KMDMC, and random CoCrNi samples and the NC *A*-atom, 350KMDMC, and random CoCrNi samples. The NC samples are included here to explore the effects of GB on microstructure evolution with respect to LD and CSRO, and to be compared with SCs.

Before shock loading, the energy of all configurations is minimized and then relaxed at 1 K or 300 K for 100 ps in the NPT ensemble with three-dimensional periodic boundary conditions (PBCs) to reach an equilibrium state. After relaxation, two vacuum regions are created at the two ends of the simulation box along the *x*-axis. This setting mimics the free boundary along *x* direction (shock direction), while PBCs remain in the transverse directions (i.e., *y* and *z* directions). A shock wave is generated by moving a virtual wall at a constant velocity U_{p} (ranging from 400 m/s to 1600 m/s for SCs and 100 m/s to 600 m/s for NCs) from one free surface of the model to the opposite surface. Owing to the driving force of GBs with high excess energy [77], plastic deformation is more easily triggered from the GBs in the NCs than interior of the SCs. Here, the largest impact velocity for the NCs is set to induce sufficient amounts of slip and nanotwin mediated plastic deformation, while at the same time avoiding the occurrence of phase transformation and local melting. The duration of virtual

Table 2
CSRO parameter α^1_{ij} of SC MEAs.

MEA/CSRO parameter	α^1_{NiNi}	α^1_{NiCo}	α^1_{NiCr}	α^1_{CoCo}	α^1_{CoCr}	α^1_{CrCr}
350KMDMC	0.4701	0.5566	0.3837	−0.0182	−0.4722	−0.1075
950KMDMC	0.1627	0.2184	0.1070	−0.0598	−0.1778	−0.1160
Random	−0.0011	0.0003	−0.0024	−0.0003	−0.0019	0.0010

Table 3
FWHM (pm) of $g(r)$ at 0, 1 and 300 K for SC *A*-atom and CoCrNi MEA samples.

T (K)FWHM (pm)Sample	350KMDMC	950KMDMC	Random	*A*-atom
0	4.7468	5.1386	5.3724	0.0110
1	4.8744	5.2918	5.5129	1.1209
300	20.2363	20.4335	20.6783	19.2374

wall movement is respectively set as 11 ps for SCs and 12 ps for NCs, which is sufficient for the sample behind the wave front to equilibrate. Then the virtual wall is removed, allowing the model to release and generate a tensile wave once the reflected rarefaction wave encounters the tail of the compression wave (i.e., the front of the release wave). A microcanonical ensemble (NVE) is applied throughout the shock simulation and the timestep size is 1 fs for all simulations.

To analyze the shock responses and physical quantities (e.g., stress, temperature, particle velocity and density), a 1-D spatial binning technique with a bin size of 10 Å is applied along the *x* direction. Results from other choices of bin sizes (5 - 10 Å) are consistent with those that will be shown here. The stress along the *x* direction (σ_{xx}) is adopted as the shock pressure and all the physical parameters are listed in Table A.1. To visualize the crystalline defects during shock simulation, we use the dislocation analysis (DXA) method [78] implemented in OVITO [79] to identify four important types of dislocations: stair-rods, Hirth locks, Shockley and perfect dislocations. The crystal analysis method of [80] is employed to characterize planar defects (i.e., stacking faults (SFs) and twin boundaries (TBs)). In the NC samples, only the intragranular lattice dislocations are taken into account in the analysis.

3. Results and discussion

3.1. Single crystalline MEA

3.1.1. Shock wave profile and plasticity initiation

We first analyze the shock response and underlying development of defects in the case of [1$\bar{1}$0]-loading for the 350KMDMC SC MEA. Fig. 2 compares snapshots of the process for U_p = 500 m/s, 800 m/s and 1200 m/s. For U_p = 500 m/s, the MEA remains elastic. Only one plateau for shock pressure σ_{xx} or shear stress τ in the shocked area develops and no plastic deformation occurs behind the elastic precursor wave. At the higher U_p = 800 m/s, while defects initiate behind the wave front, the shear stress τ in the plastic region is only partially relieved, remaining at $\sim$ 4.0 GPa in the corresponding plastic region (Fig. 2 (b)), signifying underdeveloped, or so-called immature, plastic deformation. For the highest shock velocity to U_p = 1200 m/s, a typical elastic-plastic two-wave structure develops, and hence, the Hugoniot elastic limit (HEL) [81,82] can be defined, as the dynamic yield strength or the onset of shock-induced plasticity of the material. As marked in Fig. 2 (c), the HEL is taken as the lowest stress value of the extended elastic wave plateau. Behind the elastic precursor wave in the plastic region, numerous dislocations and dissociated SFs are observed on all four planes with non-zero Schmid factors. The fluctuations seen on the extended elastic wave plateau arise from the formation of dislocation loops in the elastic-plastic transition region [83].

Fig. 2 (d-f) tracks the corresponding changes in the CSRO for these different levels of U_p. When there is no plastic deformation, such as in the cases of low U_p, the average CSRO in the material fluctuates at constant levels or only slightly decreases along the *x*-direction. When the U_p is sufficiently high for a stable plastic region to develop, the plastic wave in Fig. 2 (c) noticeably reduces the degree of CSRO (Fig. 2 (f)). The glide of dislocations drives the atoms to become more disordered [71].

To examine load-orientation dependence, Fig. 3 compares the elastic and plastic pressures for the three SC MEAs and the *A*-atom sample for the two different loading directions ([1$\bar{1}$0] and [111]) and temperatures (1 K and 300 K). For the samples remaining elastic during low-speed shock loading, only an elastic wave propagates and the elastic pressure is calculated as the averaged σ_{xx} on the elastic wave plateau. For the samples under high-speed shock loading, in which a typical elastic-plastic two-wave structure can develop, the σ_{HEL} is taken as the elastic pressure, while the plastic pressure is defined as the averaged σ_{xx} on the plastic wave plateau. For the shocked samples upon intermediate-speed loading, where the plastic deformation is immature and a stable elastic-plastic two-wave structure is absent, we do not consider the plastic pressure but only the elastic pressure, which is computed as the averaged σ_{xx} on the elastic wave plateau.

As shown in Fig. 3 (a) and (b), when the entire sample is still elastic for low shock velocities, i.e., U_p = 500 m/s or 600 m/s, the elastic pressures of all material models (three MEAs and *A*-atom) along both loading directions are almost the same at 1 K. At the other extreme, at the highest shock velocity U_p = 1600 m/s, all four material models exhibit the typical elastic-plastic two-wave structure for both loading directions. Similarly, the plastic pressures in these cases are nearly the same. The development of plasticity fully relieves the shear stress, leaving a hydrostatic compressive state in the plastic region and eliminating any anisotropy between the two SC orientations. Notable differences, however, arise in their shock resistance for the intermediate cases of shock velocity. In general, the elastic pressure of *A*-atom model surpasses MEAs at U_p = 1200 m/s in the [1$\bar{1}$0]-loading, while the random MEA (no CSRO) and *A*-atom material prove to be weaker than MEAs with CSRO, developing plasticity under the same U_p in the [111]-loading. For instance, for the [111] load direction at U_p = 800 m/s, MEAs with CSRO are still elastic, while the random MEA develops immature plasticity and *A*-atom material mature plasticity with an elastic-plastic two-wave structure. At U_p = 1200 m/s, the random MEA (no CSRO) and *A*-atom materials form the typical elastic-plastic two-wave structure but the MEAs with CSRO along the harder [111]-load direction do not.

The cases analyzed thus far were carried out at 1 K. When repeating at 300 K, we find that the trends in i) the elastic and plastic pressures with the increases in shock velocity and ii) the ranking among these pressures for the four different material systems at same shock velocity, are the same as those seen at 1 K. Only a few differences are noteworthy at U_p = 1200 m/s and 300 K (Fig. 3 (d)). The 350KMDMC and 950KMDMC models loaded along [111] develop an elastic-plastic two-wave structure and thus elastic/plastic pressures at 300 K, which are absent at 1 K. We attribute the difference to the promotion of dislocation nucleation with rising temperature.

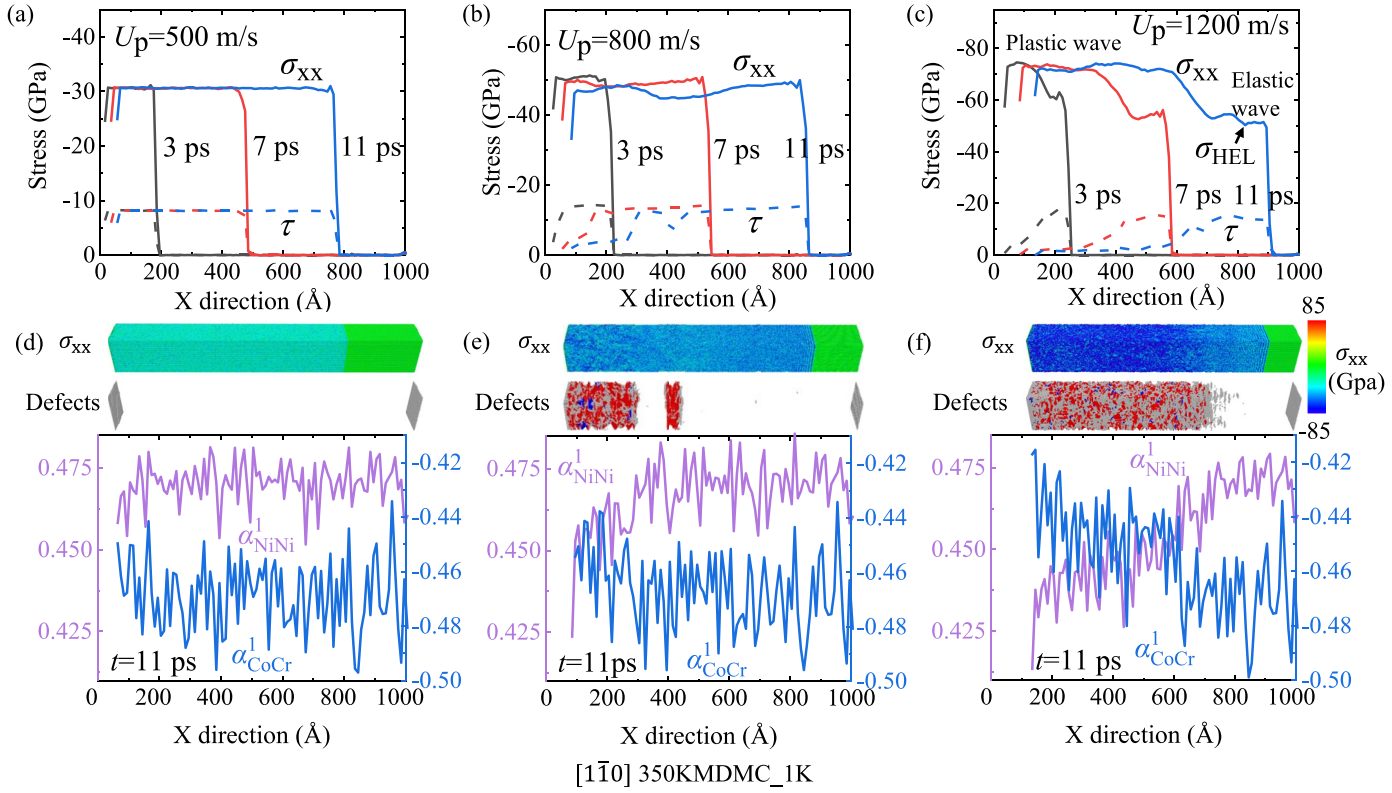

Fig. 2. (a)-(c) Evolution of the shock pressure σ_{xx} and shear stress τ of SC 350KMDMC CoCrNi MEAs under shock compression of U_p = 500 m/s, 800 m/s and 1200 m/s along [1$\bar{1}$0] orientation at 1 K, respectively. The solid lines correspond to σ_{xx}, while the dashed lines are τ. In (c), the elastic wave, Hugoniot elastic limit (HEL) and plastic wave are shown as the example. (d)-(f) The profiles of the pairwise CSRO parameters α^1_{NiNi} and α^1_{CoCr} at 11 ps. Snapshots of σ_{xx} profiles and the corresponding defect structures at 11 ps are shown for each case. Here, the atomic color scheme of defects and the definition of 350KMDMC model are consistent with those in Fig. 1. FCC atoms are removed to better visualize the defects.

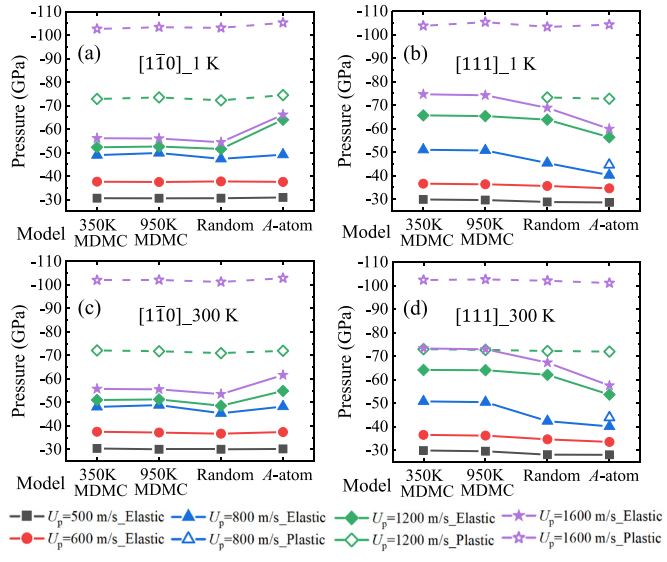

Fig. 3. Elastic and plastic pressures for three SC MEAs and the *A*-atom model at (a)-(b) 1 K and (c)-(d) 300 K shocked along [1$\bar{1}$0] and [111] directions upon different shock velocities U_p, respectively. The solid lines correspond to elastic pressures, while the dashed lines denote plastic pressures. Here, the definitions of different MEAs are consistent with those in Fig. 1, while *A*-atom refers to the model microstructure produced by the *A*-atom potential for this MEA.

The different characteristics between MEAs and *A*-atom model mentioned above imply that the onset and development of plastic deformation in these models are associated with both LD and CSRO, which can be elaborated via the analysis of the HEL.

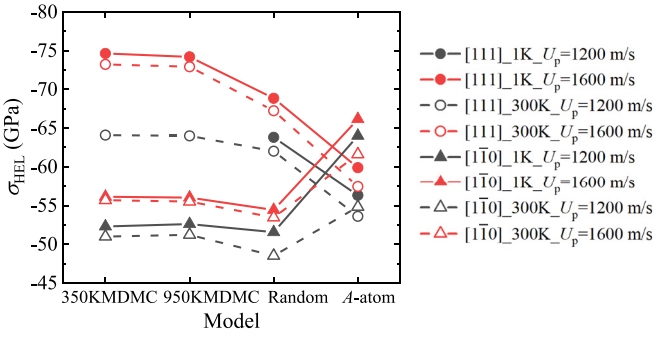

Fig. 4. The σ_{HEL} for the three SC MEAs and the *A*-atom model loaded along two crystallographic directions at 1 K and 300 K under shock compression of U_p = 1200 m/s and 1600 m/s. Here, the definitions of MEAs are consistent with those in Fig. 1, while *A*-atom refers to the mean-field model of the MEA produced by an *A*-atom potential. The solid and dashed lines represent 1 K and 300 K, respectively. Black and red symbols denote two different U_p of 1200 and 1600 m/s, respectively. Circle and triangle symbols are the loadings along [111] and [1$\bar{1}$0] directions, respectively. (For interpretation of the references to colour in this figure legend, the reader is referred to the web version of this article.)

3.1.2. The effects of LD and CSRO on HEL with respect to anisotropy

To investigate the effects of LD and CSRO on HEL of SC MEAs, we analyze the response under sufficiently high U_p = 1200 m/s and 1600 m/s (Fig. 4), in which an elastic-plastic two-wave structure formed.

To isolate the effects of LDs from those of CSRO, we first compare σ_{HEL} of the SC random CoCrNi and *A*-atom models for both loading orientations. First, regarding anisotropy, for the random MEA, σ_{HEL} along the [1$\bar{1}$0] direction is lower than that in the [111]

direction. In contrast, for the *A*-atom material, the σ_{HEL} in the [111] direction is lower than that of [1$\bar{1}$0] direction. Regarding LD effects, for [1$\bar{1}$0] loading, the random MEA has the lower σ_{HEL} than *A*-atom model. However, for [111] loading, the relation reverses. The differing anisotropy in σ_{HEL} among these cases is complicated by the fact that σ_{HEL} is sensitive to both the amounts of dislocations that can nucleate and how easy it is for them to propagate, for which both LD and orientation can affect.

For the pure *A*-atom metal, the anisotropy seen here can be expected. The same anisotropy, that is, the lower σ_{HEL} in the [111] orientation than [1$\bar{1}$0] orientation, has been reported, for instance, in previous large-scale shock compression simulations of Cu [84]. The easier plastic development in [111] loading is attributed to the larger number of stressed slip systems. For the [111] orientation, six slip systems have non-zero Schmid factors as opposed to four for the [1$\bar{1}$0] orientation, see Table 1. The applicability of Schmid's law under one-dimension strain loading condition is discussed in the supplementary material. Although the Schmid factors in [111] are lower than those in [1$\bar{1}$0], in high-stress conditions, having more suitably oriented slip systems increases the probability of plastic initiation. In initially defect-free pure metal single crystals, the HEL is governed by nucleation, not propagation, since the slip resistance to the dislocation glide that ensues after initiation is extremely low in pure FCC metals. For MEA CoCrNi, however, LD aids the nucleation of dislocations but substantially increases the slip resistance to dislocation propagation by $\sim$ 19% [71]. With propagation now being the limiting factor in MEAs, the larger Schmid factors in [1$\bar{1}$0] loading help dislocations overcome the enhanced slip resistance by offering higher resolved shear stresses than the [111] loading under the same normal shock pressure. Consequently, in the MEA, the σ_{HEL} in [1$\bar{1}$0] is lower than that in the [111], reverse from what is seen in pure metals. When the MEA and *A*-atom are both loaded in the [111] direction, the higher slip resistance in the MEA causes the higher σ_{HEL} than *A*-atom model. The opposite situation arises in the [1$\bar{1}$0], since all four systems are very well oriented for slip propagation, with nearly ideal Schmid factors. Hence, since in the random MEA with LD, dislocation nucleation is easier than in the *A*-atom material, resulting in a lower σ_{HEL}.

With the addition of CSRO to MEA, the energy barrier for dislocation nucleation and the slip resistance to dislocation propagation are enhanced compared to that of random MEA [71]. As a result, σ_{HEL} is the highest in the 350KMDMC material. Between the 350KMDMC and 950KMDMC samples, the higher degree of CSRO in the former has a mild contribution to raising the σ_{HEL}. Further, it can be shown that any MEA with the same degree of CSRO, the anisotropy in σ_{HEL}, where [1$\bar{1}$0] < [111], is the same at both 1 K and 300 K. This further confirms that the HEL in these MEAs is propagation-limited, due to the relatively higher resistance to propagation.

3.1.3. Oscillation of the elastic precursor wave

The local chemical fluctuations in MEAs not only alter the anisotropy in the HEL, but also affect some features of the waveform, manifesting as the absence of oscillations in the elastic precursor wave in the random MEA, as shown in Fig. 5, which are expected to occur, as they do in the pure *A*-atom metal.

In shock-compression loading, when wall impacts the free surface of the model, a step-pulse elastic precursor wave is generated and, as the compressive wave moves forward, the momentum transfers from one plane of atoms to another. The abrupt step-like pulse drives the atoms to fluctuate, without sufficient time for them to equilibrate after shock. This results in oscillation in the wave profile ahead of the elastic precursor wave.

In the SC *A*-atom samples, these leading oscillations develop for both loading directions at 1 K, although they are more pronounced in the [1$\bar{1}$0] loading (Fig. 5 (e)) than [111] loading (Fig. 5 (f)). As shown in Fig. 6(a), the atoms in the FCC *A*-atom model are ordered and in their ideal arrangement positions. Herein, [1$\bar{1}$0] is the closest packing direction and the distance between the neighboring (1$\bar{1}$0) planes is 1.259 Å, while the interplanar spacing of the (111) planes is 2.055 Å. Hence, shock loading along the [1$\bar{1}$0] leaves less time for the newly impacted atoms to equilibrate than those along the [111], manifesting as more severe fluctuations ahead of the elastic precursor wave. Such an orientation-dependent solitary wave train of the elastic precursor wave has been reported previously in SC Cu MD simulations when shocked in the < 110 > orientation [83–85]. On the contrary, the SC random MEAs have a more stable elastic shock front in both [1$\bar{1}$0] and [111] loading (Fig. 5 (a)-(b)) and the oscillations are absent. We suspect the deviations in atomic positions induced by the LD in random MEAs (Fig. 6 (b)), dissipate the energy when the atomic planes impact each other and mitigate the oscillation. At 300K, the oscillations have substantially reduced in the loaded SC *A*-atom sample (Fig. 5 (g–h)). Here, thermal vibrations affect atomic positions and response in a similar way as the LD, weakening the oscillations at elevated temperatures.

3.1.4. The evolution of defects

As the stress waves propagate, the material experiences three stages of deformation–first compression, then release, and finally tension–and each can lead to the development of defects, such as dislocations, stacking faults (SFs) and nanotwins. Fig. 7 compares the evolution in the TBs and SFs (Fig. 7 (a)-(c)) and four types of dislocations (Fig. 7 (d)-(f)) in the 350KMDMC material for different U_p over these three stages (marked by green, blue, and orange colored backgrounds). The other MEA materials experience a similar process, and therefore their result are not shown in the interest of space.

Consistent with the description in Section 3.1.1, for U_p = 500 m/s, no defects are generated at the compression and release stages under shock compression until the tensile wave forms via the encounter of the reflected wave from the free surface with the release tail of the compression wave (Fig. 7 (a) and (d)). As the tensile region expands, dislocation numbers increase and dislocations dissociate into partials with SFs. Ultimately, these dislocation densities decrease when the formation of voids results in material separation (e.g., Moment C in Fig. 7 (g)).

At U_p = 800 m/s, dislocations are generated at the compression stage (e.g., Moment D in Fig. 7 (h)), but partially annihilate at the release stage due to the stress relief (Moment E in Fig. 7 (h)). In the release period, the TB density slightly rises, indicating that the transformation from SFs to nanotwins via dislocation interactions also occurs in this stage (Fig. 7 (b) and (e)). Similar to the low shock velocity response from U_p = 500 m/s, the SF density also first increases in the tension stage and then decreases due to the second stress relief in the spallation region upon fracture (Moment F in Fig. 7 (h)).

At the higher U_p = 1200 m/s, complete development of plasticity is accompanied by a greater number of SPs and SFs, along with immobile dislocations, like Stair-rod and Hirth dislocations at the compression stage (Fig. 7 (c) and (f)). Bursts of mobile dislocations on multiple non-coplanar glide planes (Moment G in Fig. 7 (i)) restrict dislocation glide and promote dislocation-dislocation interactions, which fosters those reactions that produce nanotwins in the subsequent release stage (Fig. 7 (c)). In the final tension stage, fracture occurs across the material (Moment I in Fig. 7 (i)), giving rise to a rapid drop in SP density (Fig. 7 (f)).

To examine the role LD played in the observed defect evolution, we compare the defect densities of random MEA and *A*-atom model under shock compression of U_p = 1200 m/s at 1 K, a temperature where differences in LD are pronounced. For the most

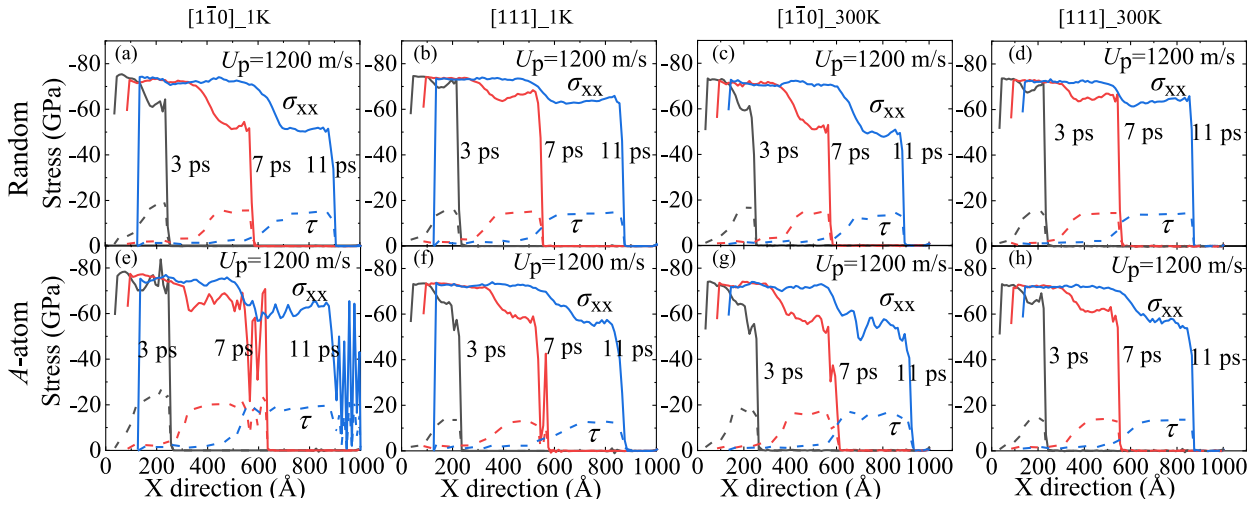

Fig. 5. Evolution of the shock pressure σ_{xx} and shear stress τ for the (a)-(d) SC random CoCrNi MEAs and (e)-(h) SC *A*-atom samples along two crystallographic directions under shock compression of U_p = 1200 m/s at 1 K and 300 K. The solid lines correspond to σ_{xx}, while the dashed lines are related to τ. Here, the definition of random model is consistent with that in Fig. 1, while *A*-atom refers to a mean-field model of the MEA produced by an *A*-atom potential.

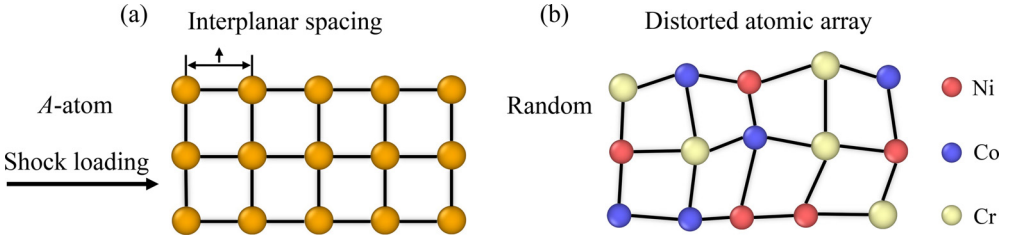

Fig. 6. Schematics of the atomic arrangement for the (a) *A*-atom material and (b) random MEA material.

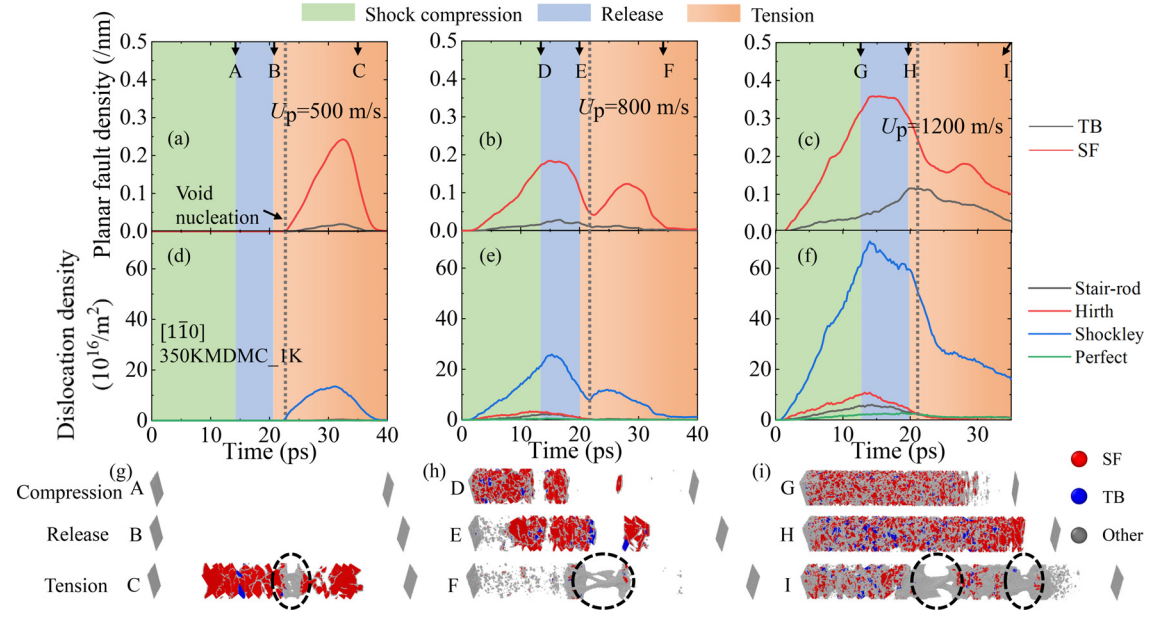

Fig. 7. Evolution of the (a)-(c) planar fault (TB and SF) densities and (d)-(f) dislocation densities for the SC 350KMDMC MEAs at U_p = 500, 800 and 1200 m/s at 1 K along the [1$\bar{1}$0] orientation. The green, blue and orange regions represent the shock compression, release and tension stages, respectively. In addition, the grey vertical dashed line in orange region denotes the moment of void nucleation at the tension stage. (g)-(i) display three representative snapshots of the defects at the shock compression, release, and tension stages, respectively under three U_p. Specifically, A, D and G are the moments when the compression wave reaches the far-end free surface; B, E and H are the ends of the release stage; C, F and I are the moments of 35 ps, where black dashed circles denote the fracture regions during tension stage. Here, the atomic color scheme of defects and the definition of model are consistent with those in Fig. 1. (For interpretation of the references to colour in this figure legend, the reader is referred to the web version of this article.)

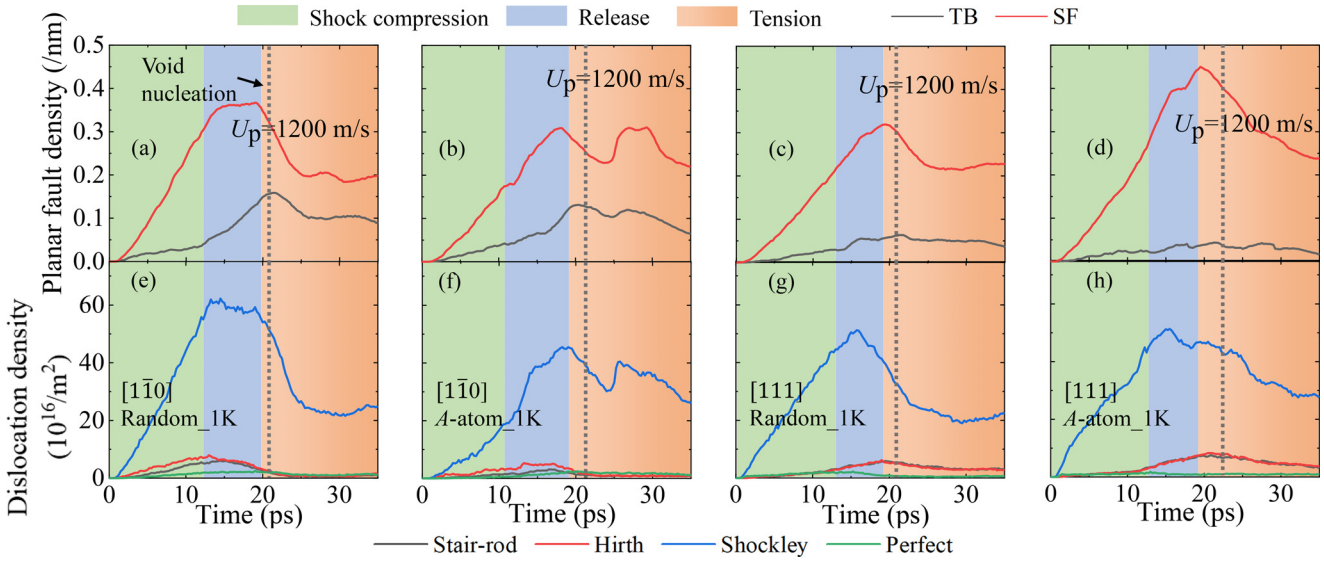

Fig. 8. Evolution of (a)-(d) planar fault (TB and SF) densities and (e)-(h) dislocation densities for the SC random CoCrNi MEA and *A*-atom model along the [1$\bar{1}$0] and [111] loading under shock compression of U_p = 1200 m/s at 1 K. The gray vertical dashed line denotes void nucleation. The definitions of random and *A*-atom models are consistent with those in Fig. 5.

part, defect evolution for these two materials is similar. As shown in Fig. 8 (a)-(d), TB densities in both samples only slightly increase at compression stage but rise faster at the release and the initial tension stages before void nucleation since glissile dislocations evolve and interact more frequently with each other at the latter two stages. In Fig. 8 (e)-(h), SP is the dominant dislocation in all cases during loading, while sessile dislocations, including Stair-rod and Hirth dislocations, evolve differently with respect to loading directions. In [1$\bar{1}$0] loading in these two samples, sessile dislocations emerge at compression stage but their densities decay later, and nearly vanish at tension stage. On the contrary, more sessile dislocations are observed at the release and tension stages than during the compression period along [111] direction. More nanotwins are, therefore, found in both the random MEA and *A*-atom samples along [1$\bar{1}$0] direction than [111] direction, since the sessile dislocations reduce the mobility of dislocations and limit chances for the reactions needed for twin formation. Comparing the TB densities between the random MEA and *A*-atom model along both directions reveals higher TB densities in the random MEA than in the *A*-atom material. The LD in the MEA aids in the formation of twins by slowing down dislocation propagation and giving rise to more chances for dislocation interactions in regions where there are few sessile dislocations.

At the higher temperature (300 K) shown in Figure S1, both random MEA and *A*-atom samples exhibit similar defect evolution as those seen at 1 K, except for the increase in twinning density for the *A*-atom exceeding that of the random MEA. In this respect, the MEA response appears to be insensitive to temperature, unlike the *A*-atom material. On the one hand, thermal vibrations at 300 K in *A*-atom play the similar role to LD in slowing down SP glide [86]. On the other hand, the temperature rise from 1 K to 300 K reduces LD in the random MEA material [71]. Consequently, for the random MEA, the aid of thermal vibration offsets the reduced LD at the higher temperature, leading to the similar amounts of twins compared to that at 1 K.

3.1.5. The CSRO-related cavitation

Once the tensile stress generated by two rarefaction waves exceeds the spall strength, voids start to nucleate at sites of weak cohesive strength or severe stress concentration. They then grow and coalesce with other voids, leading to final fracture of material. This cavitation process is the main mechanism for spallation in ductile metals.

To reveal the effects of CSRO on void nucleation during the tension stage, Fig. 9 (a) presents the hydrostatic strain distribution and α^1_{NiNi} distribution in the SC 350KMDMC MEA under shock compression of U_p = 500 m/s at 1 K prior to dislocation nucleation. The hydrostatic strain distribution is heterogeneous, and comparison of the two distributions associates the Ni segregation sites of large α^1_{NiNi} with large hydrostatic tensile strains. Since large hydrostatic strains are associated with the void nucleation [87], it is likely that the void nucleation sites correspond to the Ni segregation sites. Fig. 9 (b) supports this notion, showing a void initiating at a Ni segregation site. Further the void grows along a region of high Ni segregation, leading to a local temperature rise (Fig. 9 (c)). Comparing the lattice parameters of 350KMDMC model (3.565 Å), random CoCr mixture (3.592 Å) and pure Ni (3.507 Å) indicates that the largest lattice mismatch exists between Ni clusters and CoCr clusters. Hence, in the MEAs with CSRO, Ni regions are likely to have tensile residual stresses, while the neighboring CoCr regions compression stresses. Once the tensile pulse is generated in the shocked material, it can be partially canceled with the compression residual stress in the CoCr clusters, but enhanced by the tensile residual stress in the Ni regions, leading to easier void formation in the Ni clusters than in the CoCr counterparts.

We further examine the role of CSRO on void nucleation at different U_p. As shown in Fig. 10, the preference of void nucleation at Ni regions and the preliminary void growth along a region of high Ni segregation are validated at both U_p = 500 m/s and 1200 m/s in the SC 350KMDMC MEA. Such preference is further confirmed by tracking the evolution of CSRO in the SC 350KMDMC MEA for loading along both directions in Figure S3. A similar correlation is also found in 950KMDMC and random MEAs shown in Figure S4 and S5 of the supplementary material. However, the nucleation sites at varied U_p have different relations with defects. At U_p = 500 m/s, void initiation starts at the intersections of SFs with regions of unrecognized crystal structure (marked by black dashed ellipses in Fig. 10 (a)). With the following expansion of voids, the surrounding SFs are eliminated and turn into amorphous clusters. At U_p = 1200 m/s, numerous amorphous clusters are generated by the increasing shock pressure and more intense plastic deformation during the previous compression stage and subsequently serve as void

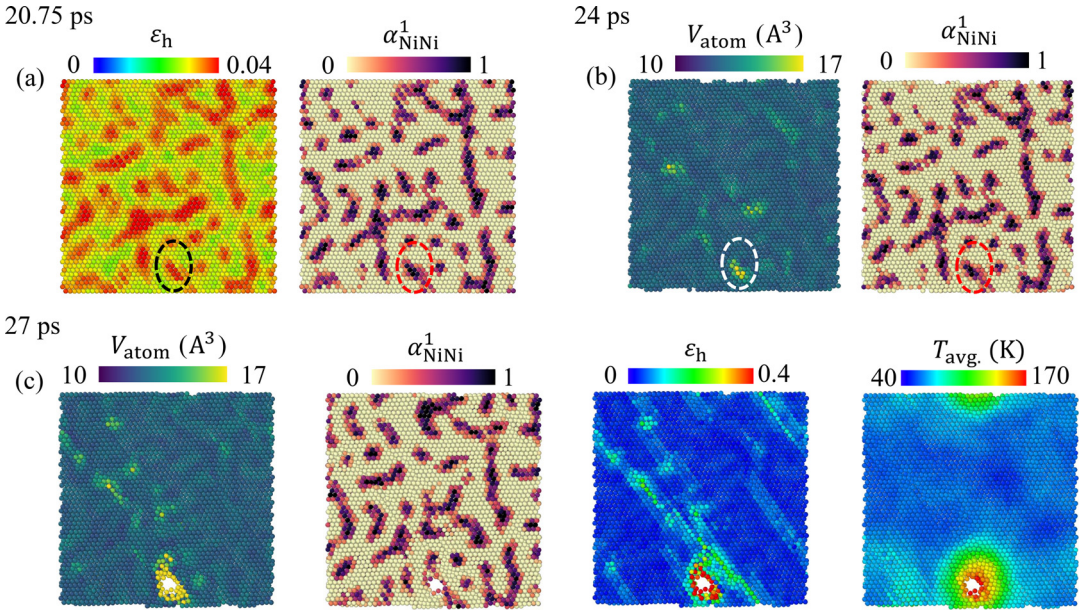

Fig. 9. Atomic distributions in the cross section of the SC 350KMDMC MEA under shock compression of U_p = 500 m/s at 1 K at (a) 20.75, (b) 24 and (c) 27 ps. The atoms are colored according to ε_h, α^1_{NiNi}, V_{atom} and $T_{avg.}$, corresponding to hydrostatic strain, CSRO, atomic volume and averaged local temperature, respectively. Dashed ellipses in (a) and (b) denote the correspondence between regions with large hydrostatic strain and Ni segregation sites, where voids prefer to nucleate. The local temperature field in (c) is obtained by the average in a sphere region with 1.2 nm radius.

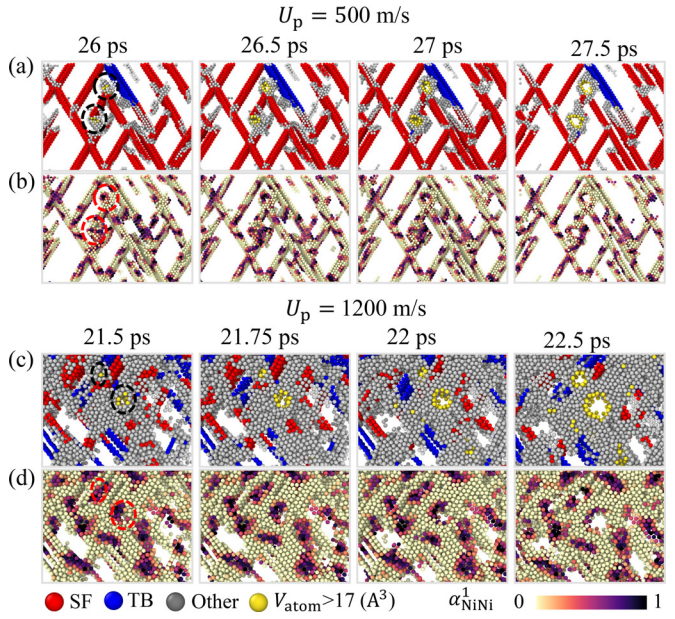

Fig. 10. Snapshots of void nucleation and growth in the SC 350KMDMC model under shock compression of (a,b) U_p = 500 m/s and (c,d)1200 m/s along [1$\bar{1}$0] at 1 K, respectively. Stacking fault (SF), twin boundary (TB), and atoms with unknown coordination structure in (a) and (c) are colored by red, blue, and gray, respectively. With the emphasis of void by dashed ellipses, the surrounding atoms of void are colored by yellow according to their atomic volume. The atomic structures in (b) and (d) are colored according to α^1_{NiNi}. (For interpretation of the references to colour in this figure legend, the reader is referred to the web version of this article.)

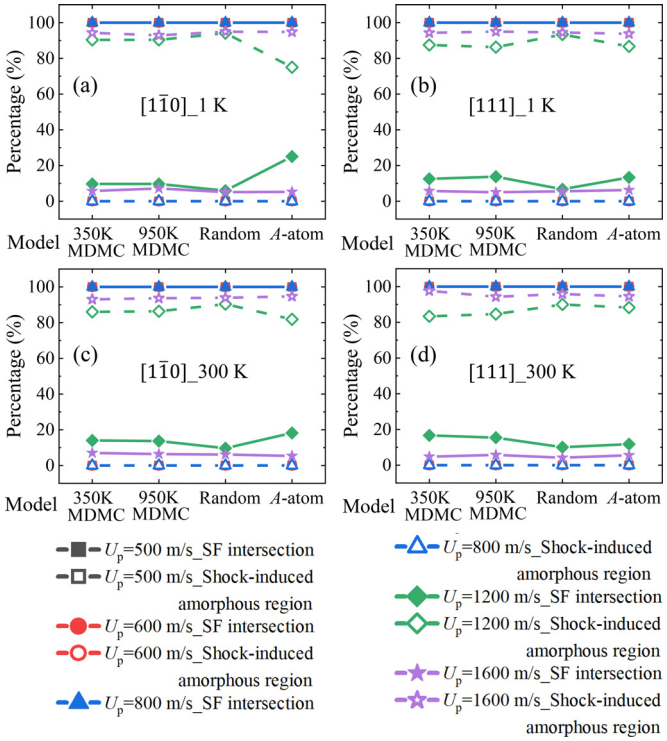

Fig. 11. The respective percentage of void nucleation event occured at the SF intersection and at the shock-induced amorphous region in SC MEAs and *A*-atom sample at different U_p. The statistic of U_p=500 m/s, 600 m/s, and 800 m/s is overlapped.

nucleation sites (marked by black dashed ellipses in Fig. 10 (c)). The voids subsequently grow in these amorphous regions during cavitation, a response also seen in Ref. [88]. Repeating the analysis for 950KMDMC and random MEAs in Figures S4 and S5 leads to the same conclusion.

To understand the role of U_p on void nucleation in SC MEAs and the *A*-atom sample, in Fig. 11, we carried out a statistical analysis to correlate the void nucleation sites with either the SF intersection points or shock-induced amorphous regions. It should be noted that the percentage of void nucleation sites that occur at a specific defect is emphasized here, rather than the percentage of a specific defect that is involved in void nucleation events. For U_p below 1200 m/s, all voids initiate at the SF intersections since nanotwinning and dislocation glide with dissociated SFs prevail when

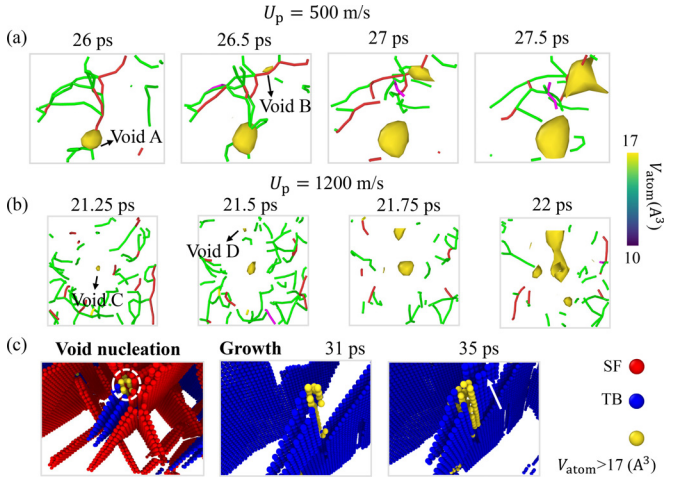

Fig. 12. Void growth (a) via dislocation adsorption at U_p = 500 m/s and (b) in the amorphous regions at U_p = 1200 m/s, and (c) suppressed by TBs. In (a), the green dislocation lines denote SP dislocation, while the red lines refer to "other" types of dislocations that do not belong to any specific type of Shockley, stair-rod, Hirth, or perfect dislocations. The void is recognized by the surface mesh algorithm (SMA) [80] and colored according to the atomic volume of the surrounding atoms. The white circle in (c) denotes the void nucleus, whose adjacent atoms have atomic volumes of larger than 17 Å^3, are colored by yellow. To better visualize the void and TBs, the SFs are eliminated at 31 and 35 ps during the void growth process in (c). (For interpretation of the references to colour in this figure legend, the reader is referred to the web version of this article.)

the shock pressure is not high enough to induce amorphous regions. At U_p = 1200 m/s, a large part of the voids in MEAs nucleate at amorphous regions induced by shock compression besides SF intersections for loadings along the two directions at both 1 K and 300 K. As the σ_{HEL} in [1$\bar{1}$0] is lower than that in [111] for MEAs, severer plastic deformation at compression stage for [1$\bar{1}$0] loading generates more amorphous regions, leading to a smaller proportion of voids nucleating at SF intersection than [111] during cavitation (see Fig. 11(a) vs (b), and Fig. 11(c) vs (d)). MEAs with CSRO possess larger σ_{HEL}, and thus the proportion of voids nucleating at SF intersection is higher than random MEA for both directions. An opposite trend is found in *A*-atom sample at U_p = 1200 m/s due to the reverse relationship between σ_{HEL} and [1$\bar{1}$0]/[111] directions. When U_p exceeds 1200 m/s, more amorphous regions initiate at the shock compression stage, which eliminates the difference of void nucleation event between two directions in all materials.

3.1.6. Void-defect interactions

Since voids are possible to nucleate either at SF intersection or shock-induced amorphous region as shown in Fig. 10 and Fig. 11, they are expected to grow through different kinds of void-defect interactions.

In Fig. 12(a) and (b), the process of void growth of SC 350KMDMC MEAs at U_p = 500 m/s and 1200 m/s is shown as examples to illustrate the difference between two kinds of void-defect interactions. For U_p = 500 m/s, void A nucleating at SF intersections grows by adsorbing the dislocations adjacent to its surface at 26 ps, which then change to residual dislocation segments at 26.5 ps. This void further expands and the surrounding dislocations are consumed entirely at 27 ps. A repeated growth process is found for void B via the same dislocation-adsorption-mediated mechanism [89–91] and these two voids can coalesce into a larger void subsequently. For U_p = 1200 m/s, void C nucleates at amorphous cluster without dislocation attached and it expands within the amorphous region until coalescing with void D formed at the neighboring amorphous region at 22 ps. Additionally, more voids are seen at 22 ps when U_p = 1200 m/s as the higher impact velocity generates larger tensile stress during cavitation and the numerous amorphous regions benefit void nucleation and expansion [88].

We also observe in simulation that closely spaced TBs can hinder void growth. As shown in Fig. 12 (c), a void nucleates at the intersection points between dislocations and nanotwins. At 31 ps, when the twinning partial dislocation glides on a parallel plane one atomic layer away from the site, a nanotwin forms on the other side of the intersection at 35 ps, denoted by the white arrow. Constrained by the TBs at both sides, the void expands anisotropically within the gap between these TBs rather than expanding radially. This constraint provided by closely spaced TBs on void growth has been reported experimentally [92,93]. The implication is that dense nanotwins formed in MEAs can hinder void expansion and coalescence.

3.2. Nanocrystalline MEA

3.2.1. Shock wave profile and HEL

For the NC samples, Fig. 13 (a)-(c) compares the shock wave profiles at 1 K at two different applied shock velocities U_p = 100 m/s and 600 m/s. The lower velocity is sufficiently small that all materials respond similarly and elastically, wherein τ remains almost constant and no dislocations or nanotwins form. The similarity among all three materials indicates that, without the formation and proliferation of defects, their intrinsic differences in LD, CSRO, and composition fluctuations do not influence the shock response. Their average elastic properties are similar and they govern the response. Furthermore, the elastic wave fronts generated in these NC tests are gentler than those generated in the single crystal tests, an expected result that has been reported in prior MD calculations of pure fcc metals [94,95] and attributed to elastic grain boundary-mediated deformation.

The higher velocity of U_p = 600 m/s is sufficiently high that an elastic-plastic wave structure develops in all three materials. The elastic-plastic plateau seen in the SC samples (Fig. 13 (d) - (f)) is absent in the NC ones, consistent with the results reported in NC Cu simulation [85]. In Fig. 13, the HEL of an NC sample is defined as the inflection point connecting the linearly rising front (elastic) and the non-linear front (plastic). The HEL is highest for the 350KMDMC material with CSRO, next for the random MEA, and lowest for the *A*-atom material. Compared to LD, the GBs, in all samples, play a far greater role in substantially reducing the energy barrier for dislocation nucleation. Thus, in NCs, the primary effect of LD and CSRO is to increase the resistance to propagation above that in a pure FCC metal. Consequently, the LD and CSRO in the MEAs lead to higher HELs than the *A*-atom material.

3.2.2. Microstructure evolution

In Fig. 14, we analyze the defect evolution under shock compression of U_p = 600 m/s at 1 K for all three materials. In the compression stage, (moment A', D' and G' in Fig. 14 (g) - (i)), extensive amounts of SPs form and glide, creating SFs. Compared to the SP densities in the SCs in the fully developed plastic regions in this same compression stage (Fig. 7 (f) and Fig. 8), the NCs contain smaller amounts of SPs and SFs. This is due not to lower rates of nucleation, but higher rates of dislocation annihilation at the GBs.

In the release stage, the glissile dislocations and SFs partially annihilate. The SF density annihilated is greatest in the 350KMDMC material, being 0.069 /nm, compared to that, 0.036 /nm, in the random MEA and 0.028 /nm in the *A*-atom. These differences are not a direct result of stress. From Fig. 13 (d) - (f), we find that the shock pressures in the stable plastic region for *A*-atom and both MEA samples are nearly the same, ~ 32 GPa. They both achieve the same hydrostatic compression state of stress. Furthermore, since the stress will be fully relieved at release stage, the stress drop is

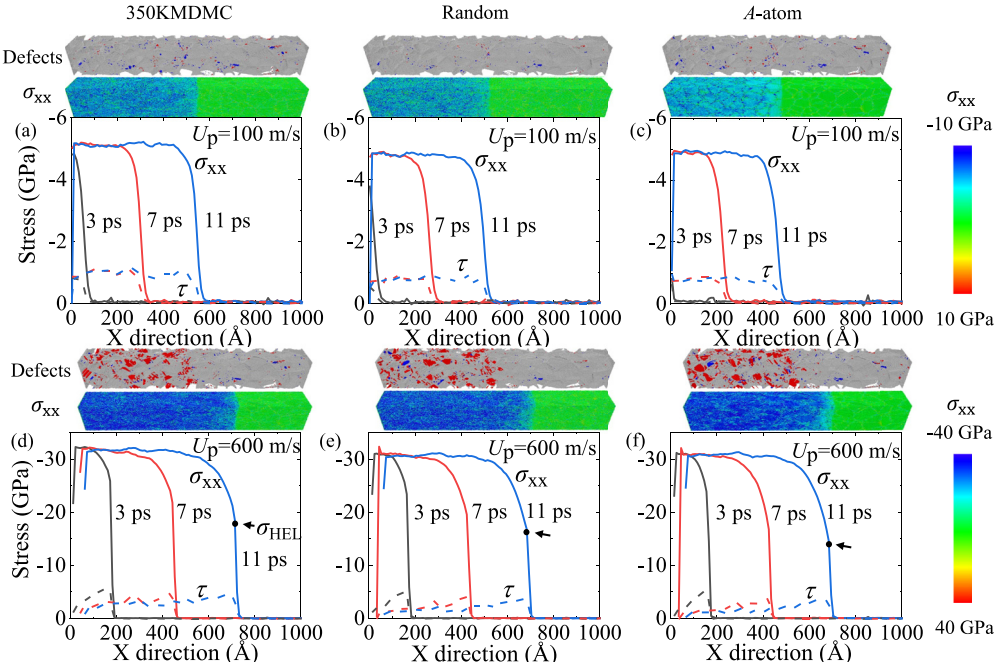

Fig. 13. Evolution of shock pressure σ_{xx} and shear stress τ in the NC ((a), (d)) 350KMDMC and ((b), (e)) random CoCrNi MEAs as well as the ((c), (f)) *A*-atom model under shock compression of U_p = 100 m/s and 600 m/s at 1 K, respectively. The solid lines correspond to σ_{xx}, while the dashed lines to τ. The HEL is indicated by black points and arrows in (d)-(f). Snapshots of the σ_{xx} profile and the corresponding defect structure at 11 ps are shown for each case. The atomic color scheme of defects is consistent with that in Fig. 1. FCC atoms are removed to better visualize the defects.

also similar among these materials. We suspect the higher rate of stacking fault annihilation seen in the 350KMDMC material than the other materials is due primarily to their differences in intrinsic stacking fault energy (ISFE). When the calculation is performed considering a large computational cross-sectional area, the 350KMDMC has the highest ISFE of 82.59 mJ/m^2, followed by the random MEA with an ISFE of -14.96 mJ/m^2, and last, the in *A*-atom with -25.26 mJ/m^2 [71]. SFs in the 350KMDMC, therefore, pose the greatest energetic penalty.

As a consequence of their different SF annihilation propensities, more SFs remain in the *A*-atom model, than in the random MEA and 350KMDMC materials after the release stage and at the start of the tension stage (Moment B', E' and H' in Fig. 14 (g) - (i)). Because nanotwins form as a result of SF-SF interactions, the highest densities of TBs are observed in the *A*-atom model and the fewest TBs are found in the 350KMDMC model in the following tension stage.

At 300 K, the trends in defect evolution and response seen in all materials are similar to those at 1 K (Figure S7). The reason is that GBs are the dominating heterogeneity that controls SP nucleation rather than LD and CSRO, and the increase in temperature affects the ISFEs for all materials in the same way. Compared to 1 K, we observe that at 300 K the TB densities of the random MEA and *A*-atom materials are still high during the release and tension stages. In contrast, fewer nanotwins are observed in the 350KMDMC material at elevated temperature. For MPEAs, samples with ISFEs below $\sim$ 21mJ/m^2 tend to favor nanotwinning [96]. Since the ISFE value of the random MEA is still negative at 300 K [97] and a similar ISFE value can be assumed in *A*-atom model, a preference for nanotwinning is maintained at 300 K. On the contrary, the 350KMDMC material lacks nanotwins since thermal effects at 300 K likely increase further its ISFE.

The spallation of NC models shows different features compared to the aforementioned SC models due to the existence of GB. As presented in Fig. 15 (a), voids in the NC 350KMDMC MEA nucleate at triple GB points with Ni segregation where the hydrostatic tensile strains are large. Next in Fig. 15 (b) and (c), after nucleation, the voids grow preferentially along the Ni segregation regions at the GBs, rather than grow and expand in the lattice as they did in the SCs. As a result, we observe that unlike the SCs, their expansion is not accompanied by a rapid decrease in SP and SF densities (Fig. 14 (a) and (d)). The CSRO evolution of α^1_{NiNi} and α^1_{CoCr} in the NC 350KMDMC MEA is tracked in Figure S8 to confirm the preferred nucleation sites at Ni region.

On the contrary, in Fig. 16, NC random MEA and *A*-atom sample do not have a preferential pathway within the Ni segregation for void growth, though voids also nucleate at triple GB junctions similar to 350KMDMC MEA. As seen in prior MD calculations of shock compression of NC pure metals [98], voids in all materials here prefer to nucleate at some specific GB sites, such as triple junctions, despite the fact that the interior of the grains are left defective after the first two stages. Accordingly, the voids grow radially during spallation in the two models without CSRO, see the spall morphology of all three models in Figure S9.

3.3. Discussion

The anisotropy in the HEL in the *A*-atom sample, the reference model, resembles those in other FCC pure metals like Cu. In these cases, the HEL anisotropy is governed by the number of activated slip systems. In pure FCC metals, where LD is absent, the atomic arrangement and structure is ordered, and the lattice resistance to dislocation glide is relatively low. Thus, the HEL corresponds to the moment of dislocation nucleation. Consequently, the [111] loading direction has lower σ_{HEL} than the [1$\bar{1}$0] loading direction in the *A*-atom material because it is oriented to activate more slip systems (six rather than four). For the random MEA, the ranking of σ_{HEL} for these two loading directions is reversed, since dislocation nucleation becomes easier and propagation harder due to the existence of LD. Hence, the process of dislocation propagation decides HEL. Compared to [111] direction, the larger Schmid factors along the [1$\bar{1}$0] direction aids dislocation glide by more suitably orient-

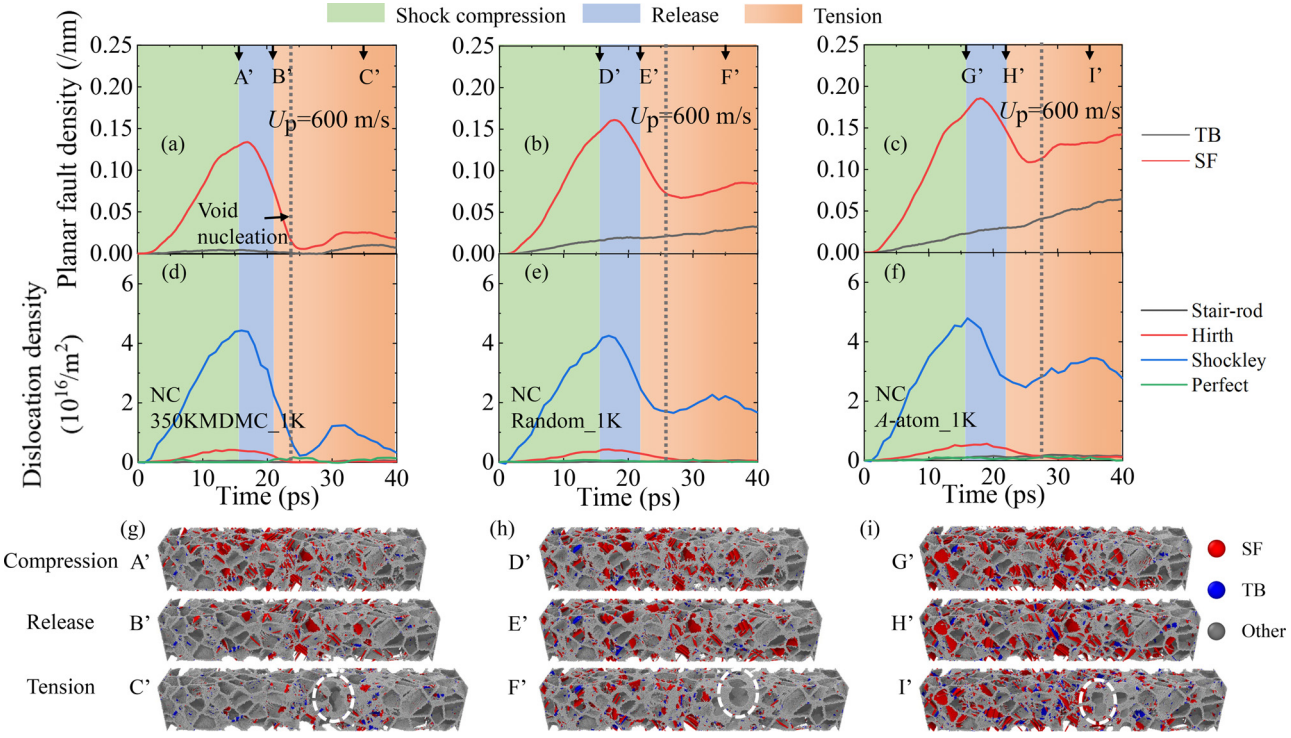

Fig. 14. Evolution of (a)-(c) planar fault (TB and SF) densities and (d)-(f) dislocation densities in the NC MEAs and *A*-atom model under shock compression of U_p = 600 m/s at 1 K. The grey vertical dashed line denotes the void nucleation event. (g)-(i) The snapshots of defects are chosen at different stages. White dashed circles denote the fracture regions during the tension stage. The atomic color scheme used for defects and the definitions of these models are consistent with those in Fig. 1. FCC atoms are removed to better visualize the defects.

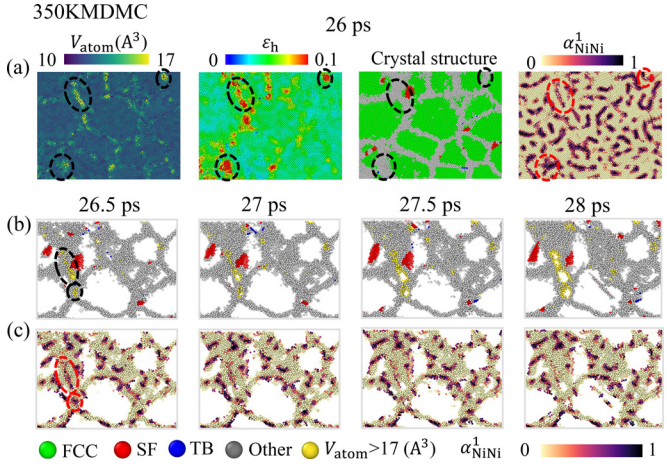

Fig. 15. (a) Void nucleation at GB with Ni segregation (denoted by dashed circles) and (b) their initial growth along GBs (denoted by dashed circles) with (c) large α^1_{NiNi} in the NC 350KMDMC MEA model under U_p = 600 m/s at 1 K. FCC atoms are removed to better visualize the GBs and defects.

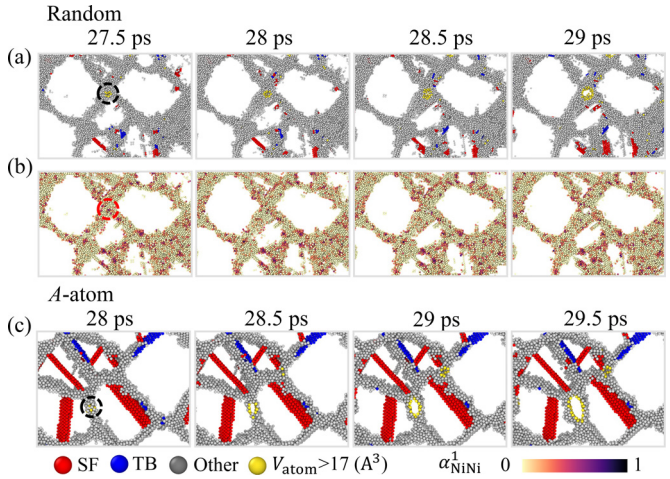

Fig. 16. (a), (c) Void nucleation at GBs (denoted by dashed circles) and their initial growth along GBs in the NC random MEA material and *A*-atom metal under U_p = 600 m/s at 1 K, respectively. (b) shows the preferential nucleation site in the random MEA material at regions with relatively large α^1_{NiNi}. FCC atoms are removed to better visualize the GBs and defects.

ing the glide planes for greater resolved shear stresses needed to overcome the slip resistance induced by LD, leading to a lower HEL.

In addition to LD, the existence of CSRO in MEA increases the HEL by raising both the energy barrier for dislocation nucleation and the slip resistance to dislocation propagation, compared to the random MEA with no CSRO. As a result, higher HEL in the 350KMDMC and 950KMDMC materials than in the random MEA arises. The notion that large resistance to dislocation motion helps enhance the HEL of MPEAs under shock loading is consistent with the recent proposal put forth by Jiang et al. [52]. Specifically, they discussed that severe local LD leads to the formation of large local elastic stress field, and the interactions between these local elastic stress fields and the stress fields of dislocations will hinder dislocation movements in MPEAs. The present work reveals that the HEL is linked with not only the dislocation nucleation event, but also the dislocation propagation process. Therefore, the roles of LD and CSRO on both nucleation and glide processes are important in understanding their collective effect on the HEL.

It has been proposed that more twins produced under shock loading can further improve the shock resistance of materials [99,100]. Here, we reveal that CSRO characteristic of some MEAs in-

directly affect the propensity for nanotwinning during shock loading. As shown in Fig. 8 and Figure S2, nanotwinning develops in the release and tension stages provided that the shock pressure is high to nucleate sufficient dislocations at the previous shock compression stage. By virtue of a higher ISFE than the random MEA or *A*-atom materials with no CSRO, the 350KMDMC sample with CSRO favors the annihilation of SFs, which reduces chances for twin formation (Fig. 7 (c)). Moreover, GBs can aid the annihilation of SFs by acting as sinks for dislocations during the release stage. Consequently, the 350KMDMC NC produces less nanotwins than these two other NC materials (Fig. 14).

In simulation, spallation begins with the nucleation and growth of voids, and for the most part, the mechanisms for both processes seen in the MEAs are similar to those reported for pure metals or conventional alloys. However, here we find that atomic-scale CSRO can influence the sites on which these processes occur. In SCs, void nucleation sites coincide with the weak amorphous zones generated either at the intersection of SFs or during the previous compression stage, as would be expected in traditional metals. We also find that another type of nucleation site exists in CoCrNi that corresponds to a relatively high degree of CSRO in Ni segregation. The strain distributions in Fig. 10 show that the regions of Ni segregation have high localized hydrostatic tensile strain, resulting from the lattice mismatch between Ni and CoCr. This reason is similar, although realized at a finer scale, to that reported in a recent study on the dynamic damage evolution of two-phase MPEAs [53], where it was found that the residual stress difference in the martensite phase and the matrix led to the preferential void nucleation site inside the matrix with tensile residual stress. In NCs, as in pure metals, voids prefer to nucleate at triple junctions. In a recent shock loading experiment of an MPEA, voids nucleated at the triple junctions of high-angle grain boundaries, coalesced and extended to the grain interior [54]. However, our simulation reveals that high CSRO for Ni segregation and its association with larger hydrostatic strain in the GBs provide an alternate preferred void growth and coalescence path. In NCs, the CSRO and ISFE of an MPEA can be properly tuned to affect the amount of nanotwinning and the spallation morphology to further improve the shock resistance of materials.

4. Conclusions

In this work, the shock-induced wave propagation, defect evolution and spallation in single crystal (SC) and nanocrystalline (NC) CoCrNi, a medium entropy alloy (MEA) are investigated using both hybrid Monte Carlo/molecular dynamics (MD) and large-scale MD simulations. The same MD calculations are repeated for an *A*-atom material, a hypothetical pure metal with the same average properties as CoCrNi, for reference. For all materials, the Hugoniot elastic limit (HEL) is obtained. The main findings are as follows.

- The HEL in the MEA exhibits an anomalous anisotropy, wherein, unlike for pure metals, the HEL in the $[1\bar{1}0]$ shock direction is lower than that in the [111] direction. The difference is attributed to lattice distortion (LD) in the MEA, which lowers the barrier for dislocation nucleation but substantially increases the resistance against dislocation propagation.
- LD aids in the formation of nanotwins by slowing down dislocation propagation in the release and tension stages, while higher degree of chemical short-range order (CSRO) increases the average intrinsic stacking fault above that of the random material and more SFs annihilate in the release stage, reducing the chances for nanotwinning.
- Voids prefer to nucleate at Ni segregation sites (with high CSRO) due to the large hydrostatic tensile strain created by the lattice mismatch between Ni and CoCr clusters. Voids initially grow in the Ni regions before further expansion and coalescence, leading to a rugged void growth path.
- In the SCs, voids nucleated at the stacking fault intersections grow by adsorbing pre-existing dislocations close to their surface, while voids initiated in shock-induced amorphization expand within these amorphous regions. In contrast, in NCs, the voids generated at triple GB junctions with high Ni CSRO grow preferentially along the GBs with Ni segregation before extending into the grain interior.

Declaration of Competing Interest

The authors declare that they have no known competing financial interests or personal relationships that could have appeared to influence the work reported in this paper.

Acknowledgements

The authors would like to thank Prof. Ryan B. Sills (Rutgers University) for helpful discussions about the void growth mechanisms. X.Y. would like to express his sincere gratitude for the financial support by National Science Foundation for Distinguished Young Scholars of China (11925203) and Natural Science Foundation of China (11672110). X.Z. acknowledges support from Natural Science Foundation of China (11972163). Z.W. gratefully acknowledges support from Natural Science Foundation of China (12072220).

Appendix A. Physical parameters

Table A1
The symbol, physical parameter and the calculation method for each quantity in this work.

Symbol	Parameter	Calculation method
σ_{xx}	Shock pressure	Binning analysis
σ_{yy}, σ_{zz}	Lateral stress	Binning analysis
τ	Shear stress	$\frac{\sigma_{xx}-(\sigma_{yy}+\sigma_{zz})/2}{2}$
σ_{HEL} / HEL	Hugoniot elastic limit	The lowest stress value of the extended elastic wave plateau (SC) / The inflection point of elastic-plastic wave profile (NC)
U_p	Particle velocity	Velocity of virtual wall
V_{atom}	Atomic volume	Voronoi method
$\epsilon_{xx}, \epsilon_{yy}, \epsilon_{zz}$	Normal strain components	–
ϵ_h	Hydrostatic strain	$\frac{\epsilon_{xx}+\epsilon_{yy}+\epsilon_{zz}}{3}$
m	Particle mass	–
N	Particle number	–
v_x, v_y, v_z	Components of velocity vector	–
v_{COM}	Local center-of-mass velocity	Binning analysis
k_b	Boltzmann constant	1.38×10^{-23}J/K
$T_{avg.}$	Average temperature of a local neighborhood with N atoms	$\frac{1}{3Nk_b}\sum_{i=1}^{N} m_i[(v_{ix}-v_{COM})^2 + v_{iy}^2 + v_{iz}^2]$

Supplementary material

Supplementary material associated with this article can be found, in the online version, at doi:10.1016/j.actamat.2021.117380

References

[1] J.-W. Yeh, S.-K. Chen, S.-J. Lin, J.-Y. Gan, T.-S. Chin, T.-T. Shun, C.-H. Tsau, S.-Y. Chang, Nanostructured high-entropy alloys with multiple principal elements: novel alloy design concepts and outcomes, Adv. Eng. Mater. 6 (5) (2004) 299–303.
[2] B. Cantor, I. Chang, P. Knight, A. Vincent, Microstructural development in equiatomic multicomponent alloys, Mater. Sci. Eng. A 375 (2004) 213–218.

[3] W. Li, D. Xie, D. Li, Y. Zhang, Y. Gao, P.K. Liaw, Mechanical behavior of high-entropy alloys, Prog. Mater. Sci. (2021) 100777.
[4] Y. Zhou, Y. Zhang, Y. Wang, G. Chen, Solid solution alloys of AlCoCrFeNiTix with excellent room-temperature mechanical properties, Appl. Phys. Lett. 90 (18) (2007) 181904.
[5] C. Lee, G. Song, M.C. Gao, R. Feng, P. Chen, J. Brechtl, Y. Chen, K. An, W. Guo, J.D. Poplawsky, et al., Lattice distortion in a strong and ductile refractory high-entropy alloy, Acta Mater. 160 (2018) 158–172.
[6] P. Shi, W. Ren, T. Zheng, Z. Ren, X. Hou, J. Peng, P. Hu, Y. Gao, Y. Zhong, P.K. Liaw, Enhanced strength–ductility synergy in ultrafine-grained eutectic high-entropy alloys by inheriting microstructural lamellae, Nat. Commun. 10 (1) (2019) 1–8.
[7] Y. Qiu, S. Thomas, D. Fabijanic, A. Barlow, H. Fraser, N. Birbilis, Microstructural evolution, electrochemical and corrosion properties of AlxCoCrFeNiTiy high entropy alloys, Mater. Des. 170 (2019) 107698.
[8] Y. Shi, B. Yang, X. Xie, J. Brechtl, K.A. Dahmen, P.K. Liaw, Corrosion of Alx-CoCrFeNi high-entropy alloys: Al-content and potential scan-rate dependent pitting behavior, Corros. Sci. 119 (2017) 33–45.
[9] N.K. Kumar, C. Li, K. Leonard, H. Bei, S. Zinkle, Microstructural stability and mechanical behavior of FeNiMnCr high entropy alloy under ion irradiation, Acta Mater. 113 (2016) 230–244.
[10] O. El-Atwani, N. Li, M. Li, A. Devaraj, J. Baldwin, M.M. Schneider, D. Sobieraj, J.S. Wróbel, D. Nguyen-Manh, S.A. Maloy, et al., Outstanding radiation resistance of tungsten-based high-entropy alloys, Sci. Adv. 5 (3) (2019) eaav2002.
[11] Z. Zhang, M. Mao, J. Wang, B. Gludovatz, Z. Zhang, S.X. Mao, E.P. George, Q. Yu, R.O. Ritchie, Nanoscale origins of the damage tolerance of the high-entropy alloy CrMnFeCoNi, Nat. Commun. 6 (1) (2015) 1–6.
[12] B. Gludovatz, A. Hohenwarter, D. Catoor, E.H. Chang, E.P. George, R.O. Ritchie, A fracture-resistant high-entropy alloy for cryogenic applications, Science 345 (6201) (2014) 1153–1158.
[13] B. Gludovatz, A. Hohenwarter, K.V. Thurston, H. Bei, Z. Wu, E.P. George, R.O. Ritchie, Exceptional damage-tolerance of a medium-entropy alloy CrCoNi CrCoNi at cryogenic temperatures, Nat. Commun. 7 (1) (2016) 1–8.
[14] S. Shukla, R.S. Mishra, Excellent high cyclic fatigue properties of a novel ultrafine-grained medium entropy alloy, Mater. Sci. Eng. A 779 (2020) 139122.
[15] T.-N. Lam, S.Y. Lee, N.-T. Tsou, H.-S. Chou, B.-H. Lai, Y.-J. Chang, R. Feng, T. Kawasaki, S. Harjo, P.K. Liaw, et al., Enhancement of fatigue resistance by overload-induced deformation twinning in a CoCrFeMnNi high-entropy alloy, Acta Mater. (2020).
[16] M.A. Hemphill, T. Yuan, G. Wang, J. Yeh, C. Tsai, A. Chuang, P. Liaw, Fatigue behavior of Al0.5CoCrCuFeNi high entropy alloys, Acta Mater. 60 (16) (2012) 5723–5734.
[17] W. Li, S. Chen, P.K. Liaw, Discovery and design of fatigue-resistant high-entropy alloys, Scr. Mater. 187 (2020) 68–75.
[18] S. Chen, W. Li, X. Xie, J. Brechtl, B. Chen, P. Li, G. Zhao, F. Yang, J. Qiao, P.K. Liaw, Nanoscale serration and creep characteristics of Al0.5CoCrCuFeNi high-entropy alloys, J. Alloys Compd. 752 (2018) 464–475.
[19] Z. Zhang, H. Sheng, Z. Wang, B. Gludovatz, Z. Zhang, E.P. George, Q. Yu, S.X. Mao, R.O. Ritchie, Dislocation mechanisms and 3D twin architectures generate exceptional strength-ductility-toughness combination in CrCoNi medium-entropy alloy, Nat. Commun. 8 (1) (2017) 1–8.
[20] J.-P. Liu, J.-X. Chen, T.-W. Liu, C. Li, Y. Chen, L.-H. Dai, Superior strength-ductility CrCoNi medium-entropy alloy wire, Scr. Mater. 181 (2020) 19–24.
[21] B. Uzer, S. Picak, J. Liu, T. Jozaghi, D. Canadinc, I. Karaman, Y. Chumlyakov, I. Kireeva, On the mechanical response and microstructure evolution of NiCoCr single crystalline medium entropy alloys, Mater. Res. Lett. 6 (8) (2018) 442–449.
[22] Y. Ma, F. Yuan, M. Yang, P. Jiang, E. Ma, X. Wu, Dynamic shear deformation of a CrCoNi medium-entropy alloy with heterogeneous grain structures, Acta Mater. 148 (2018) 407–418.
[23] G. Laplanche, A. Kostka, C. Reinhart, J. Hunfeld, G. Eggeler, E. George, Reasons for the superior mechanical properties of medium-entropy CrCoNi compared to high-entropy crmnfeconi, Acta Mater. 128 (2017) 292–303.
[24] J. Miao, C. Slone, T. Smith, C. Niu, H. Bei, M. Ghazisaeidi, G. Pharr, M.J. Mills, The evolution of the deformation substructure in a Ni-Co-Cr equiatomic solid solution alloy, Acta Mater. 132 (2017) 35–48.
[25] Y. Zhao, T. Yang, Y. Tong, J. Wang, J. Luan, Z. Jiao, D. Chen, Y. Yang, A. Hu, C. Liu, et al., Heterogeneous precipitation behavior and stacking-fault-mediated deformation in a CoCrNi-based medium-entropy alloy, Acta Mater. 138 (2017) 72–82.
[26] C. Slone, S. Chakraborty, J. Miao, E.P. George, M.J. Mills, S. Niezgoda, Influence of deformation induced nanoscale twinning and FCC-HCP transformation on hardening and texture development in medium-entropy CrCoNi alloy, Acta Mater. 158 (2018) 38–52.
[27] W. Guo, Z. Pei, X. Sang, J.D. Poplawsky, S. Bruschi, J. Qu, D. Raabe, H. Bei, Shape-preserving machining produces gradient nanolaminate medium entropy alloys with high strain hardening capability, Acta Mater. 170 (2019) 176–186.
[28] Q. Ding, X. Fu, D. Chen, H. Bei, B. Gludovatz, J. Li, Z. Zhang, E.P. George, Q. Yu, T. Zhu, et al., Real-time nanoscale observation of deformation mechanisms in CrCoNi-based medium-to high-entropy alloys at cryogenic temperatures, Mater. Today 25 (2019) 21–27.
[29] M. Naeem, H. He, F. Zhang, H. Huang, S. Harjo, T. Kawasaki, B. Wang, S. Lan, Z. Wu, F. Wang, et al., Cooperative deformation in high-entropy alloys at ultralow temperatures, Sci. Adv. 6 (13) (2020) eaax4002.
[30] J. He, Q. Wang, H. Zhang, L. Dai, T. Mukai, Y. Wu, X. Liu, H. Wang, T.-G. Nieh, Z. Lu, Dynamic deformation behavior of a face-centered cubic FeCoNiCrMn high-entropy alloy, Sci. Bull. 63 (6) (2018) 362–368.
[31] N. Kumar, Q. Ying, X. Nie, R. Mishra, Z. Tang, P. Liaw, R. Brennan, K. Doherty, K. Cho, High strain-rate compressive deformation behavior of the Al0.1CrFeCoNi high entropy alloy, Mater. Des. 86 (2015) 598–602.
[32] T. Zhang, Z. Jiao, Z. Wang, J. Qiao, Dynamic deformation behaviors and constitutive relations of an AlCoCr1.5Fe1.5NiTi0.5 high-entropy alloy, Scr. Mater. 136 (2017) 15–19.
[33] Z. Jiao, S. Ma, M. Chu, H. Yang, Z. Wang, Y. Zhang, J. Qiao, Superior mechanical properties of AlCoCrFeNiTix high-entropy alloys upon dynamic loading, J. Mater. Eng. Perform. 25 (2) (2016) 451–456.
[34] D. Foley, S. Huang, E. Anber, L. Shanahan, Y. Shen, A. Lang, C. Barr, D. Spearot, L. Lamberson, M. Taheri, Simultaneous twinning and microband formation under dynamic compression in a high entropy alloy with a complex energetic landscape, Acta Mater. 200 (2020) 1–11.
[35] J.M. Park, J. Moon, J.W. Bae, M.J. Jang, J. Park, S. Lee, H.S. Kim, Strain rate effects of dynamic compressive deformation on mechanical properties and microstructure of CoCrFeMnNi high-entropy alloy, Mater. Sci. Eng. A 719 (2018) 155–163.
[36] S. Ma, Z. Jiao, J. Qiao, H. Yang, Y. Zhang, Z. Wang, Strain rate effects on the dynamic mechanical properties of the AlCrCuFeNi2 high-entropy alloy, Mater. Sci. Eng. A 649 (2016) 35–38.
[37] B. Hopkinson, X. a method of measuring the pressure produced in the detonation of high, explosives or by the impact of bullets, Philos. Trans. R. Soc. A 213 (497–508) (1914) 437–456.
[38] R. Davies, A critical study of the hopkinson pressure bar, Philos. Trans. R. Soc. A 240 (821) (1948) 375–457.
[39] H. Kolsky, An investigation of the mechanical properties of materials at very high rates of loading, Proc. Phys. Soc. B 62 (11) (1949) 676.
[40] B.A. Gama, S.L. Lopatnikov, J.W. Gillespie Jr, Hopkinson bar experimental technique: a critical review, Appl. Mech. Rev. 57 (4) (2004) 223–250.
[41] B. Wang, A. Fu, X. Huang, B. Liu, Y. Liu, Z. Li, X. Zan, Mechanical properties and microstructure of the CoCrFeMnNi high entropy alloy under high strain rate compression, J. Mater. Eng. Perform. 25 (7) (2016) 2985–2992.
[42] K. Jiang, T. Ren, G. Shan, T. Ye, L. Chen, C. Wang, F. Zhao, J. Li, T. Suo, Dynamic mechanical responses of the Al0.1CoCrFeNi high entropy alloy at cryogenic temperature, Mater. Sci. Eng. A 797 (2020) 140125.
[43] L. Wang, J. Qiao, S. Ma, Z. Jiao, T. Zhang, G. Chen, D. Zhao, Y. Zhang, Z. Wang, Mechanical response and deformation behavior of Al0.6CoCrFeNi high-entropy alloys upon dynamic loading, Mater. Sci. Eng. A 727 (2018) 208–213.
[44] T. Zhang, S. Ma, D. Zhao, Y. Wu, Y. Zhang, Z. Wang, J. Qiao, Simultaneous enhancement of strength and ductility in a NiCoCrFe high-entropy alloy upon dynamic tension: micromechanism and constitutive modeling, Int. J. Plast. 124 (2020) 226–246.
[45] P. Lu, T. Zhang, D. Zhao, S. Ma, Q. Li, T. Wang, Z. Wang, Effects of stress states and strain rates on mechanical behavior and texture evolution of the CoCrFeNi high-entropy alloy: experiment and simulation, J. Alloys Compd. 851 (2020) 156779.
[46] Z. Li, S. Zhao, S.M. Alotaibi, Y. Liu, B. Wang, M.A. Meyers, Adiabatic shear localization in the CrMnFeCoNi high-entropy alloy, Acta Mater. 151 (2018) 424–431.
[47] Z. Li, S. Zhao, H. Diao, P. Liaw, M. Meyers, High-velocity deformation of Al0.3CoCrFeNi high-entropy alloy: remarkable resistance to shear failure, Sci. Rep. 7 (2017) 42742.
[48] S. Zhao, Z. Li, C. Zhu, W. Yang, Z. Zhang, D.E. Armstrong, P.S. Grant, R.O. Ritchie, M.A. Meyers, Amorphization in extreme deformation of the CrMnFeCoNi high-entropy alloy, Sci. Adv. 7 (5) (2021) eabb3108.
[49] M.A. Meyers, C.T. Aimone, Dynamic fracture (spalling) of metals, Prog. Mater. Sci. 28 (1) (1983) 1–96.
[50] T.P. Remington, B.A. Remington, E.N. Hahn, M.A. Meyers, Deformation and failure in extreme regimes by high-energy pulsed lasers: a review, Mater. Sci. Eng. A 688 (2017) 429–458.
[51] N. Yan, Z. Li, Y. Xu, M.A. Meyers, Shear localization in metallic materials at high strain rates, Prog. Mater. Sci. (2020) 100755.
[52] Z. Jiang, J. He, H. Wang, H. Zhang, Z. Lu, L. Dai, Shock compression response of high entropy alloys, Mater. Res. Lett. 4 (4) (2016) 226–232.
[53] Y. Yang, S. Yang, H. Wang, Effects of the phase content on dynamic damage evolution in Fe50Mn30Co10Cr10 high entropy alloy, J. Alloys Compd. 851 (2020) 156883.
[54] Y. Yang, S. Yang, H. Wang, Effects of microstructure on the evolution of dynamic damage of Fe50Mn30Co10Cr10 high entropy alloy, Mater. Sci. Eng. A (2020) 140440.
[55] J. Ding, Q. Yu, M. Asta, R.O. Ritchie, Tunable stacking fault energies by tailoring local chemical order in CrCoNi medium-entropy alloys, Proc. Natl. Acad. Sci. 115 (36) (2018) 8919–8924.
[56] S. Yin, J. Ding, M. Asta, R.O. Ritchie, Ab initio modeling of the energy landscape for screw dislocations in body-centered cubic high-entropy alloys, npj Comput. Mater. 6 (1) (2020) 1–11.
[57] Q.-J. Li, H. Sheng, E. Ma, Strengthening in multi-principal element alloys with local-chemical-order roughened dislocation pathways, Nat. Commun. 10 (2019) 3563.
[58] E. Antillon, C. Woodward, S. Rao, B. Akdim, T. Parthasarathy, Chemical short range order strengthening in a model FCC high entropy alloy, Acta Mater. 190 (2020) 29–42.

[59] F.-H. Cao, Y.-J. Wang, L.-H. Dai, Novel atomic-scale mechanism of incipient plasticity in a chemically complex CrCoNi medium-entropy alloy associated with inhomogeneity in local chemical environment, Acta Mater. (2020).
[60] Y. Zhou, Y. Zhang, F. Wang, G. Chen, Phase transformation induced by lattice distortion in multiprincipal component $CoCrFeNiCu_xAl_{1-x}$ solid-solution alloys, Appl. Phys. Lett. 92 (24) (2008) 241917.
[61] H.S. Oh, D. Ma, G.P. Leyson, B. Grabowski, E.S. Park, F. Körmann, D. Raabe, Lattice distortions in the FeCoNiCrMn high entropy alloy studied by theory and experiment, Entropy 18 (9) (2016) 321.
[62] L. Owen, E. Pickering, H. Playford, H. Stone, M. Tucker, N. Jones, An assessment of the lattice strain in the CrMnFeCoNi high-entropy alloy, Acta Mater. 122 (2017) 11–18.
[63] Y. Zhao, T. Nieh, Correlation between lattice distortion and friction stress in Ni-based equiatomic alloys, Intermetallics 86 (2017) 45–50.
[64] Y. Zhao, Z. Lei, Z. Lu, J. Huang, T. Nieh, A simplified model connecting lattice distortion with friction stress of Nb-based equiatomic high-entropy alloys, Mater. Res. Lett. 7 (8) (2019) 340–346.
[65] R. Zhang, S. Zhao, J. Ding, Y. Chong, T. Jia, C. Ophus, M. Asta, R.O. Ritchie, A.M. Minor, Short-range order and its impact on the CrCoNi medium-entropy alloy, Nature 581 (7808) (2020) 283–287.
[66] B. Yin, W. Curtin, Origin of high strength in the CoCrFeNiPd high-entropy alloy, Mater. Res. Lett. 8 (6) (2020) 209–215.
[67] X. Chen, Q. Wang, Z. Cheng, M. Zhu, H. Zhou, P. Jiang, L. Zhou, Q. Xue, F. Yuan, J. Zhu, W. Xiaolei, E. Ma, Direct observation of chemical short-range order in a medium-entropy alloy, Nature 592 (2021) 712716.
[68] F. Wang, G.H. Balbus, S. Xu, Y. Su, J. Shin, P.F. Rottmann, K.E. Knipling, J.-C. Stinville, L.H. Mills, O.N. Senkov, et al., Multiplicity of dislocation pathways in a refractory multiprincipal element alloy, Science 370 (6512) (2020) 95–101.
[69] L.T. Smith, Y. Su, S. Xu, A. Hunter, I.J. Beyerlein, The effect of local chemical ordering on frank-read source activation in a refractory multi-principal element alloy, Int. J. Plast. 134 (2020) 102850.
[70] S. Xu, Y. Su, W.-R. Jian, I.J. Beyerlein, Local slip resistances in equal-molar MoNbTi multi-principal element alloy, Acta Mater. (2020).
[71] W.-R. Jian, Z. Xie, S. Xu, Y. Su, X. Yao, I.J. Beyerlein, Effects of lattice distortion and chemical short-range order on the mechanisms of deformation in medium entropy alloy CoCrNi, Acta Mater. 199 (2020) 352–369.
[72] S. Plimpton, Fast parallel algorithms for short-range molecular dynamics, J. Comp. Phys. 117 (1) (1995) 1–19.
[73] W.-R. Jian, L. Wang, W. Bi, S. Xu, I.J. Beyerlein, Role of local chemical fluctuations in the melting of medium entropy alloy CoCrNi, Appl. Phys. Lett. 119 (12) (2021) 121904.
[74] W. Brostow, J.-P. Dussault, B.L. Fox, Construction of voronoi polyhedra, J. Comput. Phys. 29 (1) (1978) 81–92.
[75] J. Cowley, An approximate theory of order in alloys, Phys. Rev. 77 (5) (1950) 669.
[76] D. de Fontaine, The number of independent pair-correlation functions in multicomponent systems, J. Appl. Crystall. 4 (1) (1971) 15–19.
[77] J.W. Bae, J.B. Seol, J. Moon, S.S. Sohn, M.J. Jang, H.Y. Um, B.-J. Lee, H.S. Kim, Exceptional phase-transformation strengthening of ferrous medium-entropy alloys at cryogenic temperatures, Acta Mater. 161 (2018) 388–399.
[78] A. Stukowski, V.V. Bulatov, A. Arsenlis, Automated identification and indexing of dislocations in crystal interfaces, Modelling Simul. Mater. Sci. Eng. 20 (8) (2012) 085007.
[79] A. Stukowski, Visualization and analysis of atomistic simulation data with OVITO–the open visualization tool, Modelling Simul. Mater. Sci. Eng. 18 (1) (2009) 015012.
[80] A. Stukowski, Computational analysis methods in atomistic modeling of crystals, JOM 66 (3) (2014) 399–407.
[81] G.I. Kanel, S.V. Razorenov, V.E. Fortov, V. Fortov, Shock-wave phenomena and the properties of condensed matter, Springer Science & Business Media, 2004.
[82] M.A. Meyers, Dynamic behavior of materials, John wiley & sons, 1994.
[83] Q. Xiong, T. Shimada, T. Kitamura, Z. Li, Selective excitation of two-wave structure depending on crystal orientation under shock compression, Sci. China Phys. Mech. Astron. 63 (11) (2020) 1–13.
[84] T.C. Germann, B.L. Holian, P.S. Lomdahl, R. Ravelo, Orientation dependence in molecular dynamics simulations of shocked single crystals, Phys. Rev. Lett. 84 (23) (2000) 5351.
[85] E.M. Bringa, A. Caro, Y. Wang, M. Victoria, J.M. McNaney, B.A. Remington, R.F. Smith, B.R. Torralva, H. Van Swygenhoven, Ultrahigh strength in nanocrystalline materials under shock loading, Sci. 309 (5742) (2005) 1838–1841.
[86] D.L. Olmsted, L.G. Hector Jr, W. Curtin, R. Clifton, Atomistic simulations of dislocation mobility in Al, Ni and Al/Mg alloys, Modelling Simul. Mater. Sci. Eng. 13 (3) (2005) 371.
[87] J.R. Rice, D.M. Tracey, On the ductile enlargement of voids in triaxial stress fields, J. Mech. Phys. Solids 17 (3) (1969) 201–217.
[88] Y. Ashkenazy, R.S. Averback, Shock induced amorphization as the onset of spall, Appl. Phys. Lett. 86 (5) (2005) 051907.
[89] R.B. Sills, B. Boyce, Void growth by dislocation adsorption, Mater. Res. Lett. 8 (3) (2020) 103–109.
[90] H.-J. Chang, J. Segurado, J. LLorca, Three-dimensional dislocation dynamics analysis of size effects on void growth, Scr. Mater. 95 (2015) 11–14.
[91] P. Noell, J. Carroll, K. Hattar, B. Clark, B. Boyce, Do voids nucleate at grain boundaries during ductile rupture? Acta Mater. 137 (2017) 103–114.
[92] S.-T. Tsai, P.-C. Chiang, C. Liu, S.-P. Feng, C.-M. Chen, Suppression of void formation at Sn/Cu joint due to twin formation in cu electrodeposit, JOM 71 (9) (2019) 3012–3022.
[93] C.-L. Huang, W.-L. Weng, C.-N. Liao, K.-N. Tu, Suppression of interdiffusion-induced voiding in oxidation of copper nanowires with twin-modified surface, Nat. Commun. 9 (1) (2018) 1–7.
[94] H. Van Swygenhoven, P. Derlet, Grain-boundary sliding in nanocrystalline fcc metals, Phys. Rev. B 64 (22) (2001) 224105.
[95] W. Ma, W. Zhu, F. Jing, The shock-front structure of nanocrystalline aluminum, Appl. Phys. Lett. 97 (12) (2010) 121903.
[96] S. Huang, W. Li, S. Lu, F. Tian, J. Shen, E. Holmström, L. Vitos, Temperature dependent stacking fault energy of FeCrCoNiMn high entropy alloy, Scr. Mater. 108 (2015) 44–47.
[97] S. Huang, H. Huang, W. Li, D. Kim, S. Lu, X. Li, E. Holmström, S.K. Kwon, L. Vitos, Twinning in metastable high-entropy alloys, Nat. Commun. 9 (1) (2018) 1–7.
[98] M.A. Meyers, S. Traiviratana, V. Lubarda, D.J. Benson, E.M. Bringa, The role of dislocations in the growth of nanosized voids in ductile failure of metals, JOM 61 (2) (2009) 35.
[99] O. Grässel, G. Frommeyer, Effect of martensitic phase transformation and deformation twinning on mechanical properties of Fe-Mn-Si-Al steels, Mater. Sci. Technol. 14 (12) (1998) 1213–1217.
[100] E.K. Salje, Ferroelastic materials, Annu. Rev. Mater. Res. 42 (2012) 265–283.